DEVELOPMENT OF LOCAL TRANSIENT HEAT FLUX MEASUREMENTS IN AN AXISYMMETRIC HYBRID ROCKET NOZZLE

A Thesis
presented to
the Faculty of California Polytechnic State University,
San Luis Obispo

In Partial Fulfillment
of the Requirements for the Degree
Master of Science in Mechanical Engineering

by
Christopher Richard D'Elia
February 2015

COMMITTEE MEMBERSHIP

TITLE:	Development of Local Transient Heat Flux Measurements in an Axisymmetric Hybrid Rocket Nozzle
AUTHOR:	Christopher Richard D'Elia
DATE SUBMITTED:	February 2015
COMMITTEE CHAIR:	William R. Murray, PhD Professor of Mechanical Engineering
COMMITTEE MEMBER:	Joseph Mello, PhD Professor of Mechanical Engineering
COMMITTEE MEMBER:	James Scott Patton, PhD Associate Professor of Mechanical Engineering

ABSTRACT

Development of Local Transient Heat Flux Measurements in an Axisymmetric Hybrid Rocket Nozzle

Christopher Richard D'Elia

A method of performing local transient heat flux measurements in an uncooled axisymmetric hybrid rocket nozzle is presented. Surface temperatures are collected at various axial locations during short duration tests and post processed using finite difference techniques to determine local transient heat fluxes and film coefficients. Comparisons are made between the collected data and the complete Bartz model. Although strong agreement is observed in certain sections of the nozzle, ideal steady state conditions are not observed to entirely validate the Bartz model for hybrid rocket nozzles. An experimental error analysis indicates the experimental heat fluxes are accurate within ±5.2% and supports the accuracy of the results.

ACKNOWLEDGMENTS

I would like to thank Dr. Murray, Dr. Mello, Dr. Patton, Dr. Shollenberger, Laad Caine, and Dr. Lemieux for their guidance throughout all stages of this project. Separately, I would like to thank Jim Gerhardt for generously lending his time and experience to the success of this project. For serving an orthogonal role to the previous supporters, I would like to thank Andrew Brock for being a solid wingman. Unquestionably, I owe a great thanks to my family, but specifically, I would like to thank my dad, Richard D’Elia, for his continuous technical expertise and relentless passion. Finally, I would like to thank all the previous members of the Cal Poly Hybrid research group for their work leading up to this thesis.

TABLE OF CONTENTS

APPENDICES

LIST OF TABLES

LIST OF FIGURES

1. INTRODUCTION

1.1 Objective

The objective of this project is to implement, quantify, and validate heat flux measurements on the Cal Poly Hybrid Rocket Motor test stand for the further development of rocket nozzles and cooling systems. Various analytical modeling techniques are presented that can be used in conjunction with the presented experimental results.

1.2 Motivation

Further design and development of cooled hybrid rocket motors will require both analytical models as well as proven methods of empirical measurement. For each design revision, models and changes must be verified experimentally by various performance tests. Specifically, heat fluxes throughout the nozzle must be measured and managed by appropriate cooling methods. However, prior to the development of sophisticated cooling methods or nozzle geometries, a fundamental understanding of the heat flux measurement must be present for validating any analytical work.

The underlying motivation for this project was to perform an ‘energy balance’ using the Cal Poly hybrid rocket motor test facility. With the overarching goal to develop cooling systems for hybrid rocket motors using nitrous oxide, an in-house means of quantifying the thermal loads on specific components is necessary. This project uses a simple converging-diverging nozzle equipped to measure the heat flux at 12 stations. Results are validated using the well known 1-D Bartz equations adapted from Reference 1 and a 2-D axisymmetric CFD model. Presumably, these techniques could be applied to other components and used to validate associated models ultimately leading to the complete design of cooled hybrid motor components.

1.3 Unit Convention

Consistent units are used in each aspect of the presented analytical and experimental work; however, different unit systems are used where applicable. Design and fabrication of the experimental apparatus is performed using traditional Imperial units to be compatible with the existing hardware. The calibrated data acquisition system reports temperatures in Fahrenheit, pressures in pounds per square inch, and weights in pounds. The material properties and thermal analyses are reported in the preferred SI unit system. Unfortunately, the complete Bartz model presented in Reference 1 is developed using traditional Imperial units, so values were converted such that processed data could be compared in SI units.

1.4 Nomenclature

The nomenclature below is used throughout the presented work.

ρ – *Density*
c_p – *Specific Heat Capacity*
T – *Temperature*
t – *Time*
r – *Radius*
k – *Thermal Conductivity*
Δt – *Time Increment*
Δr – *Radial Increment*
q_f – *Surface Heat Flux*
h_g – *Surface Film Coefficient*
T_o – *Free Stream Gas Temperature*
T_w – *Wall Temperature*
$\dot{m}$ – *Total Mass Flowrate*
g_o – *Gravity*
p_1 – *Chamber Pressure*
A_t – *Throat Area*
c^* – *Characteristic Velocity*
$\dot{m}_o$ – *Oxidizer Mass Flowrate*
$\dot{m}_f$ – *Fuel Mass Flowrate*
R – *Oxidizer to Fuel Ratio*
p_o – *Exit Pressure*
γ – *Ratio of Specific Heats*
G_o – *Oxidizer Mass Flux*
A_p – *Port Area*
$\dot{r}$ – *Regression Rate*
μ – *Viscosity*
μ_o – *Viscosity at Inlet*
T_{oi} – *Inlet Free Stream Temperature*
y^+ – *Dimensionless Wall Distance*
y – *Wall Distance*
c_f – *Skin Friction Coefficient*
U – *Free Stream Velocity*

2. BACKGROUND

As a starting point for this research, the techniques described in Reference 1 and 2 used to validate the Bartz equations were considered. Ideally, Cal Poly would have a similar set of experimental methods and equipment.

The experimental setup used to validate the Bartz equations consisted of two distinct categories of thermocouple junctions used in uncooled nozzles; Reference 2 discusses these two methods in detail. First, a set of embedded surface junctions was placed in the body of a simple converging-diverging nozzle. These junctions were designed to measure the fluid film temperature inside the nozzle. Second, a set of exposed outer surface junctions were placed in corresponding locations on the outer surface of the nozzle. To compute the heat flux and fluid film coefficient, these two sets of temperatures were used as boundary conditions in a simple radial heat conduction problem.

Since the relevant conduction/diffusion equation is nonlinear when considering variable specific heat and thermal conductivity, simple finite difference methods were applied. These difference equations were evaluated for each set of temperatures: inner and outer surface. Then, the temperature gradient could be approximated and used to approximate the heat flux and fluid film coefficient.

Two types of embedded thermocouple plugs were successfully tested according to the methods described above. The principal goal in each design was to introduce the thermocouple junction without disturbing the local heat conduction. The first design involved modifying a Delta Couple, a commercially available surface junction sketched in Figure 1. The Delta Couple featured thermocouple wires embedded axially in a solid metal plug. These plugs were pressed into the body of the nozzle and cut to match the profile of the nozzle. Following installation, the junction itself was formed on the surface with an electro-less nickel plating.

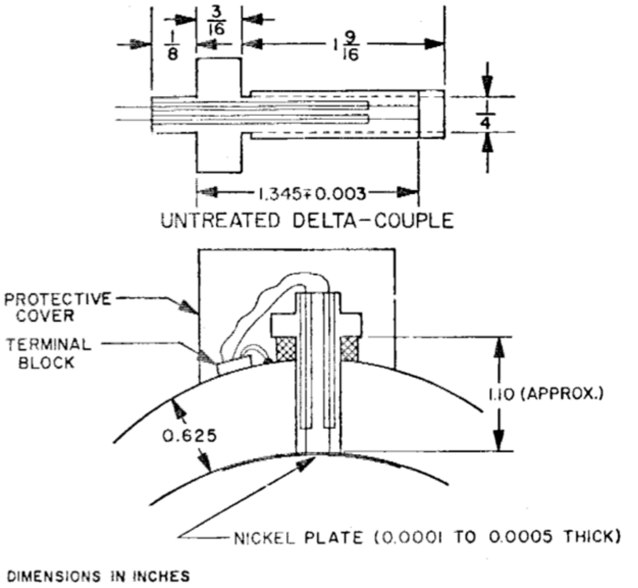

Figure 1. Delta-Couple illustration from Reference 2.

The second method involved embedding a small thermocouple junction just behind the surface of the nozzle using 36 gauge wires routed down grooves on either side of a cylindrical plug. Just before the surface of the nozzle, the grooves were terminated at 0.0145" holes aimed towards the middle of the plug, where the junction itself was formed as presented in Figure 2. A small amount of material, referred to as a web, was left in between the holes such that the wires could be resistance welded to the plug. Similar to the plated Delta-Couple method described above, this method introduced a third metal, in this case the steel web, which was assumed to be at the indicated temperature. Since the junction itself was formed behind the surface of the nozzle, a small extrapolation was used to determine the surface temperature and associated gradient. With a corrected surface temperature and temperature gradient, the heat flux and film coefficient could be calculated.

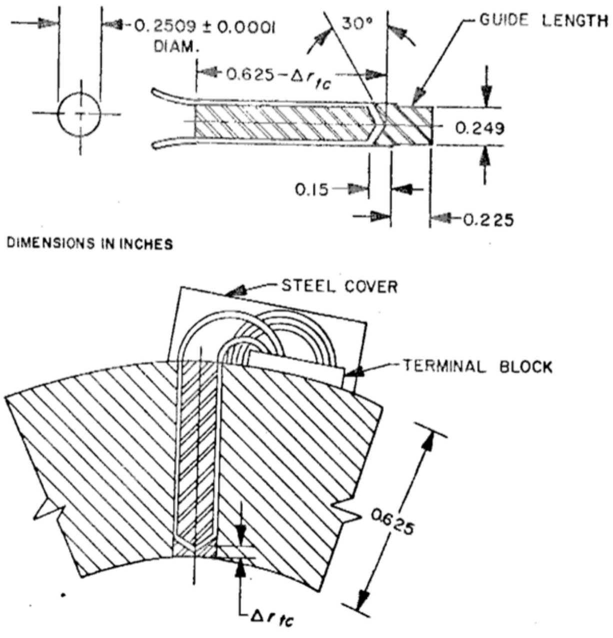

Figure 2. Recessed thermocouple junction illustration from Reference 2.

3. EXPERIMENTAL DESIGN

3.1 The Evolution of the Thermocouple Plug

Considering the manufacturing capabilities available at Cal Poly and the current commercial unavailability of Delta-Couples or similar devices, the thermocouple plug method detailed in Figure 2 was selected.

Initial attempts were made to develop robust methods of manufacturing the thermocouple plugs according to the dimensions in Reference 2. Primarily, manufacturing tests began with accurately drilling the two 0.0145" holes used to route the thermocouple wires to the junction. Readily available 12L14 free-machining ground shaft material was used for these tests. With the head tilted on a vertical milling machine and the 0.250" stock held in a 5C collet block, these holes could easily be drilled manually using an eye loop. Carbide drills were used mostly to avoid wandering at the 0.143" depth, but they also cut much faster and smoother than HSS drills. Sectioning the stock after drilling showed that the holes could be drilled to the proper depth and could be made to meet at the center of the stock. Extreme caution was taken to ensure that the drill was centered over the 5C collet block such that the block could be removed and rotated to drill opposing holes without changing the setup. Any misalignment relative to the centerline of the stock was doubled since the fixture was inverted to drill the second hole. Misalignment was visible on sectioned plugs as the two holes did not meet in the center to form the desired 0.010" web.

With some thermocouple plugs drilled, thermocouple welding tests were performed using fiberglass insulated 36 gauge K type thermocouple wire. Though both wires, Chromel and Alumel, are slightly different alloys, they are both predominantly nickel based and can be welded to steel. Rather than fabricating a capacitive discharge welder as described in Reference 2, a Hughes Aircraft spot welder was used. Reference 2 describes using a spring-loaded jig to hold the wire in place while welding it to the plug; however, prior to fabricating a jig, a series of trial welds were performed manually. Unfortunately, specialized resistance welding equipment for thin wires, similar to what is described in Reference 3, was not suitable for welding the wires in the center of the plug. Since the 36 gauge wires needed to be welded to a 0.010" web inside the plug, some wires were test welded to 0.010" steel shim stock. This initial test immediately demonstrated the difficulty associated with welding these wires, as the joints were commonly cold or extremely brittle. Similar tests were also performed with 30 gauge wires with much more encouraging results.

A spring-loaded jig then was constructed to support the wires during the welding process. This jig could be setup in two distinct configurations for the welding process where the collet always served as one electrode. The sprung jig could either act as one electrode in the welding process, which required that the thermocouple wire be bare close to the end of the hole, or the jig could simply support the plug and wire assemblage, while the electrode was attached to a remote end of the thermocouple wire.

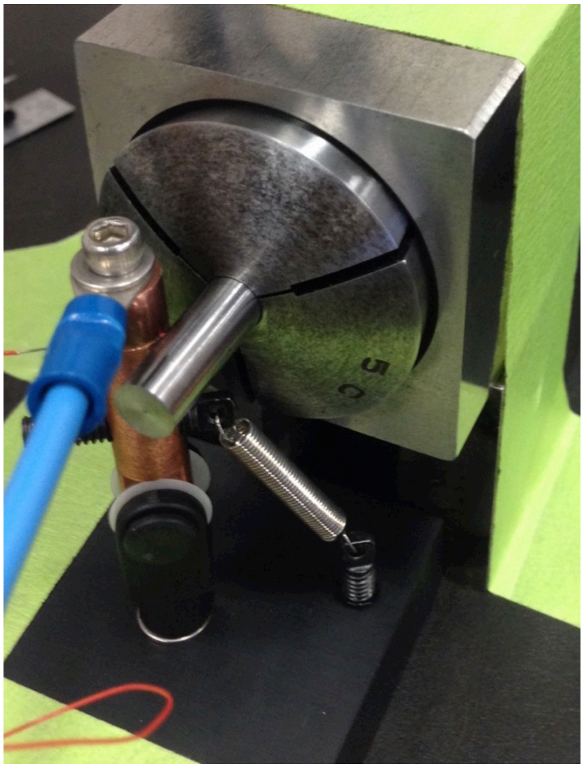

Figure 3. Thermocouple wire resistance welding fixture. The sprung copper fixture served as one electrode while the collet block was used to connect the second electrode.

Throughout the welding tests, it was found that Chromel wire required significantly more heat to weld than Alumel wire and thus needed to be welded first. This implied that a substantial amount of the weld energy is dissipated into the first wire while the second wire is welded. Also, since the wire itself serves as the electrode between the outer wall of the plug and the web where the weld is performed, a DCEN or direct current electrode negative configuration of the spot welder is recommended. This allows the most energy to be put into the weld before the wire melts back or sublimates.

Ultimately, neither jig configuration produced an ideal result with the 36 gauge wire; however, some success was seen with the 30 gauge wire. If the wires could be stripped close to the hole, the spring loaded jig and spot welder could be used to weld the wires to the web inside the plug. Though resistance welding was promising, connecting the electrode required removing and reinstalling insulation such that the wires could be potted against the steel plug body. Alternatively, short gauged lengths of wire could be used as described in Reference 2. With a short length of wire, the weld could be performed with one electrode connected to the free end of the wire, leaving the insulation in tact along its length. The main difficulty seen with this method involved manipulating the 1.000" length without damaging the wire, insulation, or weld. Though feasible with the 30 gauge fiberglass insulated wire, a more repeatable, accurate, and robust junction design was desired.

While exploring other similar small welding applications, laser welding was presented as an alternative. Unfortunately, the plug was not designed such that the laser could be focused directly on the weld area. Since the guide length of the plug was designed as a sacrificial section to be removed following installation in the nozzle body, it became apparent that material could be removed from the guide end to expose the weld area. Initial tests with a laser welder were performed on existing plugs whose guide length was bored out to 0.125". Between the guide length and the junction, a small 0.0625" bore was made to expose the thermocouple wire holes. With these modifications, the two thermocouple wires could be routed through their respective holes and into this clearance area. The laser welder melted them back to fill the 0.0625" bore and form the junction. Tests were performed with the 30 gauge and 36 gauge wire to demonstrate feasibility of this concept; however, the main issue revealed the need for extra filler material to completely fill the small bore back to the nozzle surface. The advantages included the ability to visually confirm a successful weld and the freedom to make the wires any length.

Ultimately, impatience and limited access to laser welding equipment led to the testing of TIG or tungsten inert gas welding. Initial tests with TIG welding were extremely promising; the high frequency start feature could be used to form traditional bead junctions. Early tests with TIG welding were performed on the same blanks made for laser welding. Though the results were promising and similar to the laser welding, the arc was frequently drawn to the surrounding guide material rather than the desired junction location. Successful welds, similar to the one in Figure 4, could be formed manually, but variable operator dexterity often resulted in overheating the thermocouple plug and burning the fiberglass insulation.

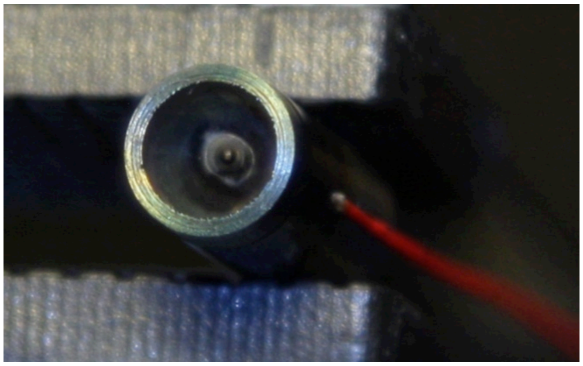

Figure 4. Early thermocouple plug welded using a TIG welder with foot pedal control. The large heat effected zone and overheated weld area is evident by the blue coloring and dull weld finish.

Simple solutions were available for each of these problems. To avoid arcing the inside of the guide length, the back of the plug was cleared out to 0.1875" using a ball end mill and the guide length was shortened from 0.200" to 0.100". The ball end mill removed ample material surrounding the weld area while avoiding the material that would ultimately form the nozzle wall. To avoid backfilling a large bore with filler material, a 0.03125" ball end mill was used to form the small bore up to the two thermocouple holes. A 0.005" chamfer was placed in-between these bores to facilitate installation of the thermocouple wires.

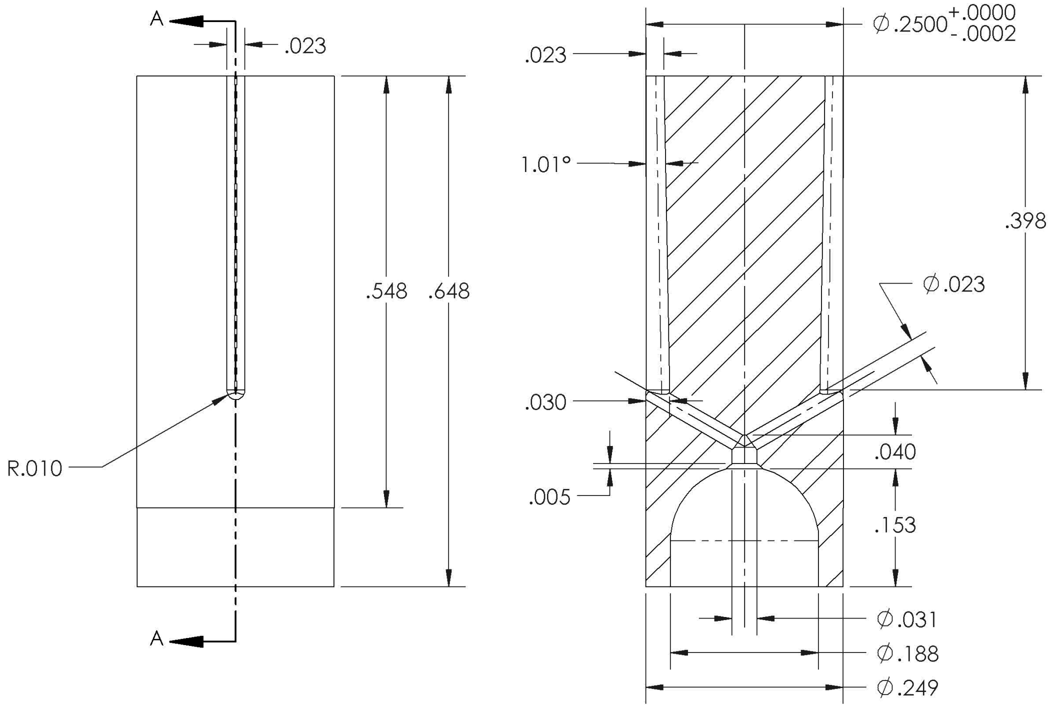

Figure 5. Final thermocouple plug design drawing with section view showing internal features. Dimensions are in inches.

The length of thermocouple wire was determined by calculating the amount of filler material required to backfill the inner bore. The two thermocouple wires were stripped to expose the correct amount of filler material and installed into the plug. After cleaning all the components thoroughly with acetone, a high frequency arc was used to melt the wires into a bead at the base of the clearance bore. To avoid overheating the wires, a 0.3s spot timer was used melt the bead into the small bore at 45A in an Argon-rich environment. Operator dexterity problems were eliminated by clamping the welding torch in place leaving an arc gap of approximately 0.050" between the tungsten and the previously formed bead. The thermocouple plug was simply held in place using a bench vise as pictured in Figure 6.

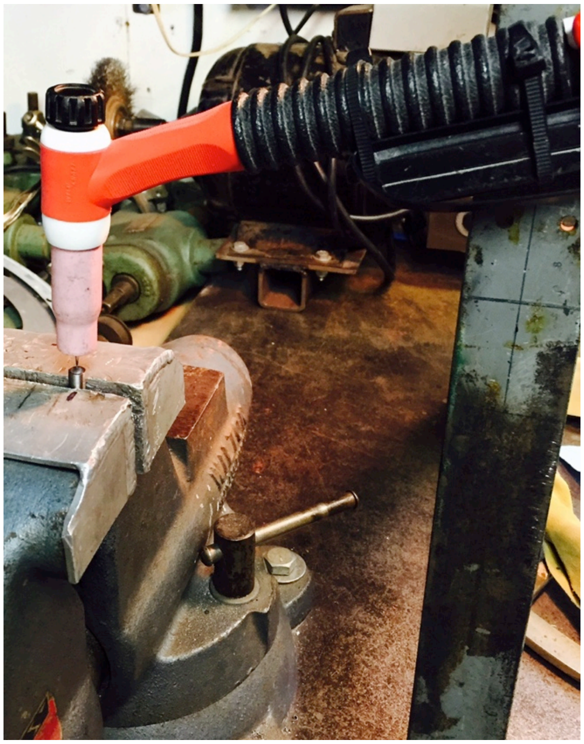

Figure 6. Thermocouple wire welding fixture. The TIG welding torch was clamped in place while the plug was fixture in a grounded bench vice with soft jaws. A special background tungsten was used to keep the arc far away from the plug wall.

This method proved extremely successful and the welds could be visually inspected to ensure that all the filler material was completely melted into the small bore. Also, sectioning a successful weld demonstrated that the filler material completely filled the small bore, effectively replacing any material that was previously removed. Despite the successful appearance of this method, there was concern that the extra material removal and larger thermocouple wires, junction, and holes would compound to substantially reduce the overall accuracy of the device by disrupting the conductive path. However, an updated finite element model was created and demonstrated the opposite. Increasing the junction size and backfilling the area with weld material significantly improves the predicted temperature reading. Theoretically, the new design introduces fewer disturbances to the conductive path than the original design presented in the Reference 2. The new design also permits longer leads outside the nozzle and heavier gauge wires, which are stronger and easier to work with.

Completing the new plug design required improvement to permit routing the larger wires out of the nozzle wall through the two corresponding grooves. Since the 30 gauge wire does not permit the same bending radius as the 36 gauge wires, the grooves required extra depth at the bend to create allowance for the larger wires to pass without being sheared by the nozzle wall on installation. This shearing effect was discovered during initial installation tests of plugs featuring straight grooves. On installation, the insulation/wires could be severed by the nozzle wall material.

With the wire size, routing, and welding technique determined, the thermocouple wire holes were reduced to the smallest available drill size that permitted installation of the fiberglass insulated wires. Drill sizes tested included 0.020", 0.0225", 0.023", and 0.024", and ultimately, a 0.0225" drill was selected to permit easy wire routing while minimizing the material removed near the surface of the nozzle.

3.2 Thermocouple Plug Finite Element Modeling

In parallel with the fabrication tests, a simple finite element model was developed to study the effects of moving from 36 gauge to 30 gauge wire since most of the features required enlargement to accommodate the larger wire. This model was inspired by the uncertainty analysis presented in Reference 2 where Powell crudely guesses at the inner boundary temperature uncertainty. Powell assumes that the temperature is unknown within 100°F; thus, the uncertainty of the inner surface temperature measurement due to unknown junction placement or an interrupted conductive path is crudely estimated to contribute 10% to the overall uncertainty.

Holding the junction location in place, a series of finite element simulations were compiled to study the effects of the thermocouple junction on the conductive path through the nozzle wall. By removing material from plug to accommodate the thermocouple wires and junction, the conductive path through the nozzle wall becomes obstructed, which causes the material to heat locally. The local heating of the junction area theoretically causes the thermocouple to indicate a temperature higher than would be present in material without a junction.

Three different geometries were studied in a pure conduction analysis: the 36 gauge wire geometry used in Reference 2, drawn in Figure 2 and modeled in Figure 7, the same geometry modified for 30 gauge wire, and the 30 gauge geometry modified for TIG welding, drawn in Figure 5. A quarter of the thermocouple plug was modeled from the measurement surface back 0.250" with all the junction details included. Perfect conduction between the weld material and the base metal was assumed. The model also assumes the wire was routed down the center of the hole with ideal insulation to a perfect weld.

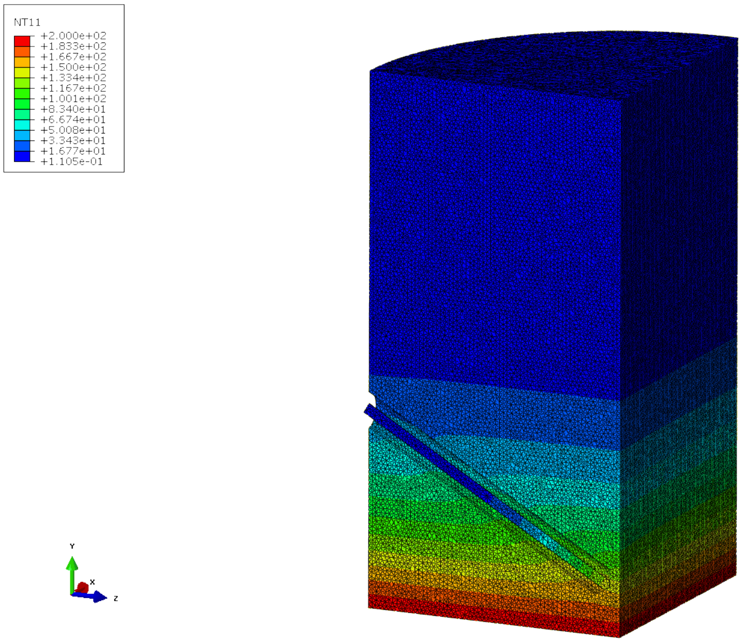

Figure 7. Thermocouple FEA model with features for 36 gauge wire showing domain, mesh, and temperature distribution.

Since the thermocouple plugs and nozzle assembly will never reach steady state, a short duration transient analysis was conducted on a 0.1s interval. This interval represents roughly twice the normal sampling interval used during in the experimental tests presented. During this interval, the measurement surface was held at 200°C. The remaining surfaces were considered insulated and given 0°C initial temperature. The field or body of the thermocouple plug was started at 0°C initial temperature.

The temperature dependent properties of steel, summarized in Table 4, were used for the body of the thermocouple plug. With one side of the thermocouple junction formed form Chromel and the other formed from Alumel, some assumptions had to be made about the wire/weld material properties. Since Alumel tends to have a higher thermal diffusivity in the range of temperatures observed, all the wire and weld material was assumed to have properties similar to Alumel. Also, since the operating conditions are close to the Currie point of Chromel, the material properties would be known with significantly less certainty. Temperature dependent properties for Alumel were taken from Reference 4 and summarized below in Table 1.

Table 1. Material properties from Reference 4 used to model Alumel wire and weld regions in the thermocouple plug finite element simulation.

Temperature [°C]	Specific Heat [J/kg-K]	Thermal Conductivity [W/m-K]
-23.15	438	27.7
1.85	452	28.5
26.85	464	29.2
51.85	476	29.9
76.85	489	30.6
101.85	501	31.1
126.85	515	31.6
151.85	510	31.9
176.85	502	32.6

The thermocouple plug geometries were discretized into solid tetrahedral elements since meshing the complex geometry surrounding the thermocouple holes with hexahedral elements was not necessary for thermal analysis. For the 30 gauge geometry modified for TIG welding, the thermocouple wire was discretized into solid hexahedral elements due to its simple geometry. A series of mesh convergence studies were conducted to establish that the junction temperature was converged with 0.005 °C over the 0.1s period. The results of these studies, summarized in Figure 8, indicated that a mesh seed size of 0.05mm or 0.03mm was acceptable.

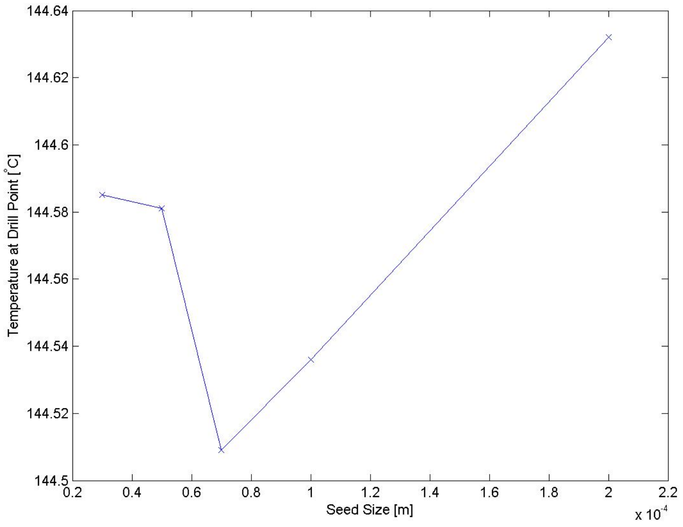

Figure 8. Convergence study performed on the geometry designed for 36 gauge wire indicating convergence at 0.05mm.

After establishing an acceptable seed size, the final simulations were compiled for each geometry. Figure 9 through Figure 11below include temperature contours for each geometry focused on the region of interest after the 0.1s simulation time.

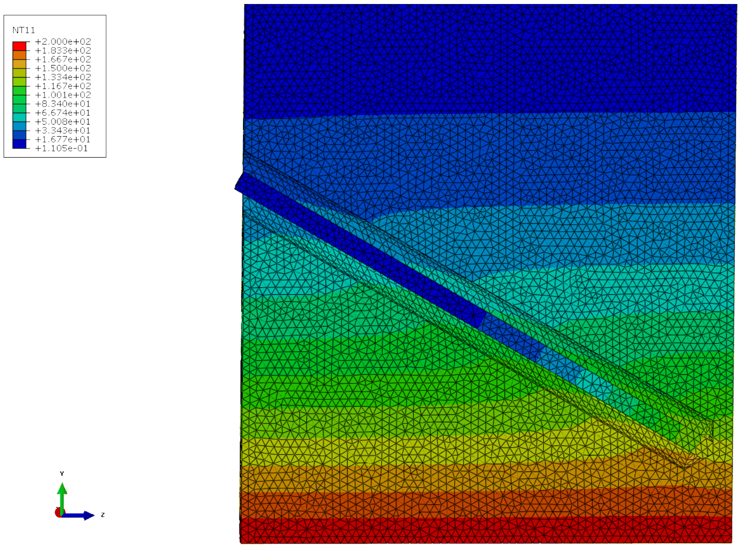

Figure 9. Simulated temperature contour in the thermocouple plug designed for 36 gauge wire.

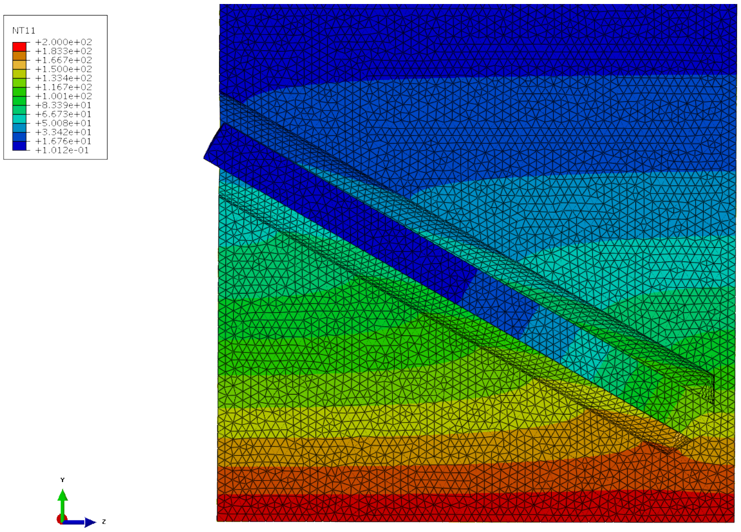

Figure 10. Simulated temperature contour in the thermocouple plug modified for 30 gauge wire

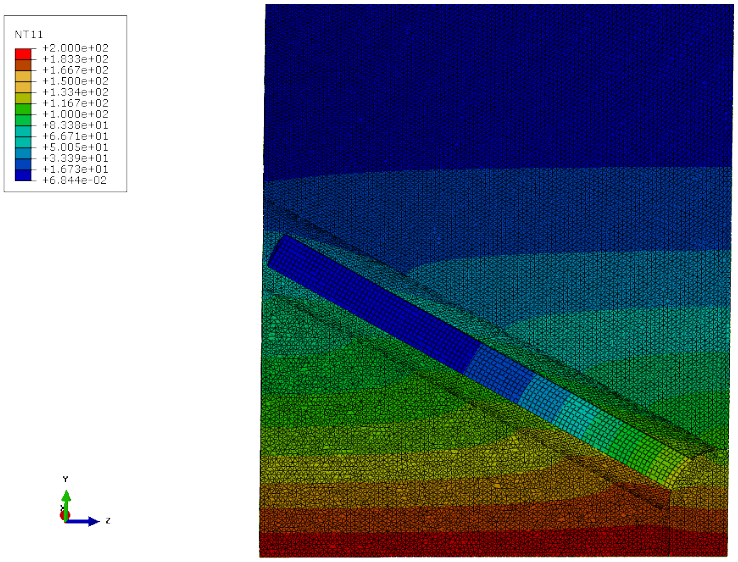

Figure 11. Simulated temperature contour in the thermocouple plug modified for TIG welding.

Following each simulation, the core temperature distribution in each geometry was reported. The core temperature is considered the temperature along the center axis of the plug. These temperature distributions are plotted in Figure 12 along with the ideal distribution, which does not contain a junction. The data indicates that in the span of the junction the 30 gauge modified geometry produces results extremely close to the ideal distribution despite the later observed deviation.

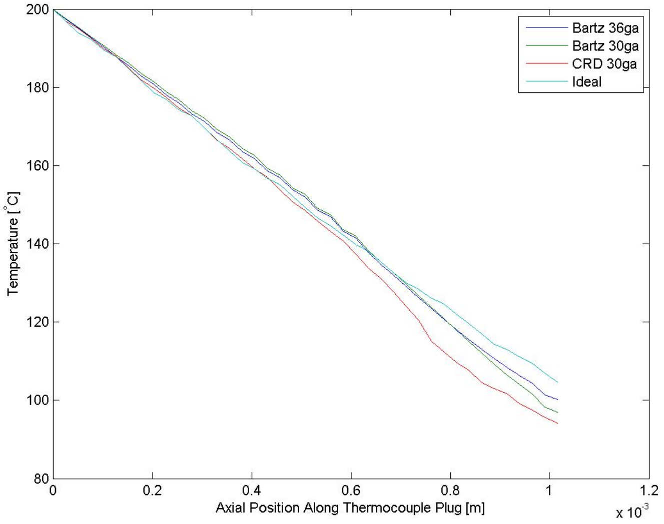

Figure 12. Core temperature distribution for each geometry analyzed. The distribution is only shown for the first 1.0mm of the plug since this area contains the surface, located at 0.0mm and the junction located at roughly 0.6mm.

Since the thermocouple junction cannot be considered smaller than the wire forming it, a single nodal temperature cannot be reported as the junction temperature. The reported junction temperature is assumed to be the average core temperature where the wires meet the center of the plug. All the junctions are centered 0.023" behind the surface, which makes the junction temperature the average core temperature from 0.018" to 0.028" for the 30 gauge wire. These junction temperatures are summarized in Figure 13. The Alumel introduced into the conductive path of the thermocouple junction lowers the simulated junction temperature below the ideal value; however, the errors reported in Figure 14 indicate that the 30 gauge geometry modified for TIG welding still produces a measurement closest to the actual temperature.

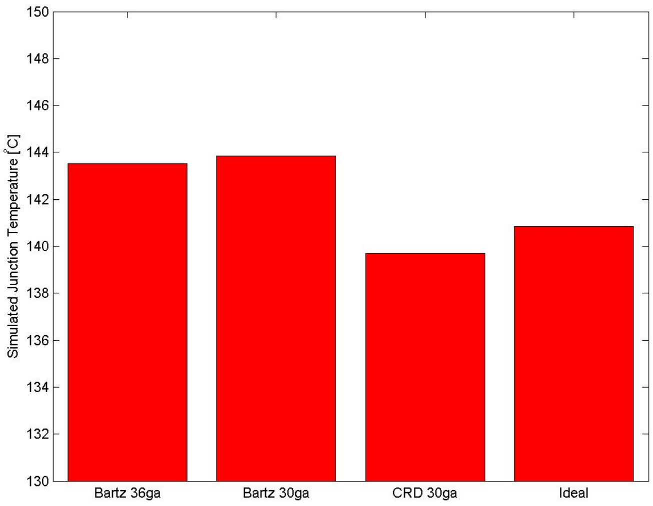

Figure 13. Simulated junction temperature for each geometry in the finite element study.

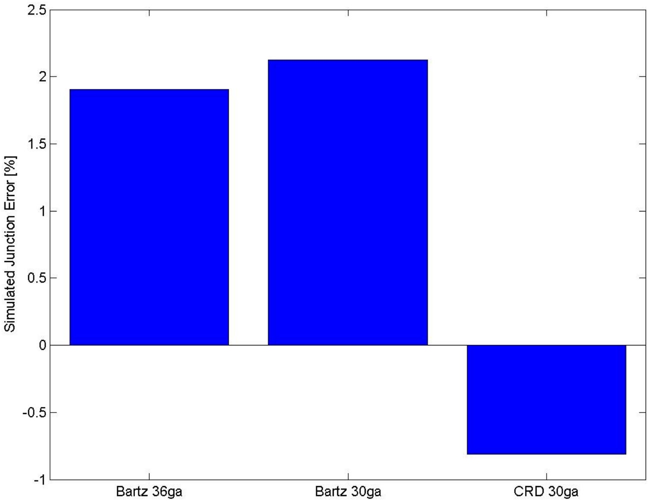

Figure 14. Simulated junction temperature error resulting from the material removed in order to introduce the thermocouple junction.

Although this analysis provides crucial insight into the nature of the embedded thermocouple plug behavior at a reasonable operating point for the presented tests, the results cannot be extended to all operating points. Simulations performed at different surface temperatures and over different durations imply that the measurement error is transient and diminishes as the entire junction is heated. For this reason, an operating point was selected to indicate a reasonable value for the error introduced during the experimental tests presented. These results indicate that the junction placement contributes an uncertainty; however, using this FEA model, another calibration could be performed to adjust the recorded temperature values to reflect the true surface temperature. Understandably, the junction location tolerance also produces a direct uncertainty on the inner surface temperature; however, these effects were studied independently by computing their influence on the final results.

3.3 Manufacturing the Thermocouple Plugs

With an acceptable plug design completed, the manufacturing process was designed to produce a minimum of 12 plugs that could be installed in the body of a converging-diverging rocket nozzle to accurately measure the surface temperature. To avoid the introduction of added lead, 1018 carbon steel was selected over the previous 12L14 that was used for prototyping. This required that the plug material be custom ground to the specified tolerances for the press fit into the nozzle body. A quick review of the finite element simulations revealed that knowing the junction location relative to the nozzle wall with certainty is important when computing the heat flux or film coefficient. This uncertainty is a direct result of the large thermal gradient expected at the surface of the nozzle: small changes in junction location can produce variations in temperature measurement.

To prevent an accumulation of tolerances by repositioning the plug for each drill, bore, and mill operation, the plug manufacturing was divided into two separate operations. The first setup started with an extra long blank of ground shaft material and handled all the critical dimensions. A 5-axis CNC mill held the blank in a 5C collet and was used to reposition the plug into different orientations to cut each of the features in the first setup. To begin, the blank was faced to length such that the other features could be made accurately from a single end. Ultimately, this would be the end used to locate the plug in the nozzle assembly. Once faced to length, the plug was tipped up so that the two thermocouple wire holes could be drilled 60 degrees from the axis of the plug. After drilling the first hole, the part was rotated to drill the opposite hole. Following the drilling of both holes, the part was rotated back down to horizontal and the first of the two slots was cut from the end of the plug to the base of the hole. Again, the part was rotated to cut the slot on the opposite side. By capturing all these features in a single setup, the location of the holes and ultimately the junction relative to the end of the plug are known within the setup tolerances of the machine.

With the critical features cut, the part was removed and installed with the faced end inside the collet. This allowed the less critical dimensions to be cut from the opposite side. First, the plug was faced to length horizontally. Once at the final length, the plug was repositioned vertically and the guide length was cut. Finally, a series of 3 ball end mills performed the final clearance bores and chamfers for the welding operations.

Approximately 30 plugs were made and the best 13 were welded and prepared for final assembly in the nozzle. One of the plugs was sectioned to check that the weld completely filled the small bore before the remaining 12 were pressed into to the nozzle body.

3.4 Design and Manufacture of the Nozzle Body

Since the heat flux measurement technique quickly became the focus of this project, the nozzle geometry itself became less important as an outcome of any theoretical or experimental work. A nozzle geometry was adopted such that theoretical heat fluxes could be calculated and compared to experimental work. Since Reference 1 presents excellent experimental results using a simple converging-diverging nozzle with a radiused inlet and straight 30 degree included angle diverging section, this geometry was adopted. The contraction ratio was selected after reviewing the published experimental results in Reference 2 and reviewing the nozzle geometries previously used on the Cal Poly hybrid test stand.

Assuming that the nozzle inlet was selected as the outer fuel grain diameter, these nozzle geometries produced substantially larger throats than ever tested on the Cal Poly hybrid test stand. Initial calculations were performed according to Reference 3 to determine the expected chamber pressures given the range of available oxidizer mass flow rates. Fuel mixture was assumed similar to previous runs implying that the fuel regression rate would not be substantially affected by the nozzle contraction ratio or chamber pressure. These calculations indicated that these nozzles could be choked using an annular PMMA[1] fuel grain, which has been extensively tested on the Cal Poly hybrid test stand. Examining the results in Reference 6 for both the 4:1 and 8:1 nozzle geometry led to the selection of the 4:1 nozzle since more data with better agreement was published. It was assumed that less agreement was seen on the 8:1 nozzle since the contraction was more aggressive and contained steeper angles incident to the flow. The general geometry was scaled such that the fuel grain exit diameters served as the nozzle inlet diameter. The values in Table 2, corresponding to Figure 15, summarize the geometry tested according to Reference 6 and the scaled geometry used on the Cal Poly hybrid stand.

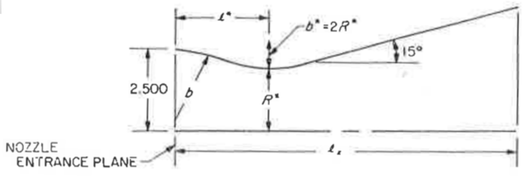

Figure 15. Generalized nozzle geometry diagram from Reference 6.

---

[1] PMMA refers to the plastic, poly(methyl methacrylate), more commonly called acrylic.

Table 2. Nozzle dimensions taken from Reference 6 and scaled to fit the Cal Poly hybrid stand. All dimensions are given in inches.

	Entrance	b	L*	R*	le
4:1 Bartz Nozzle	2.500	2.500	3.312	1.250	7.050
4:1 Cal Poly	1.593	1.593	2.110	0.797	4.492

The nominal 0.625" wall thickness used in the Reference 2 was originally considered despite the rest of the geometry being scale down. However, after reviewing the Marman clamp dimensions on the Cal Poly hybrid test stand, a 0.500" wall thickness appeared optimal to avoid stepping a thicker wall down around the clamp flange. Though the 0.500" wall thickness appeared to create a much cleaner design, the press fit tolerances were scrutinized to avoid ejecting the thermocouple plugs at high chamber pressures and temperatures.

The press fit tolerances for the plugs were designed to ensure that even under the highest chamber pressures and worst case dimensions, the plugs would remain in the nozzle. The force required to hold the plug in place at the highest chamber pressure was determined to be less than 20lb. Though this force is rather small and does not drive the fit dimensions directly, extremely tight tolerances were required to ensure that a tight press fit was always achieved. The potential thermal effects were not considered due to the scope of the project; rather, the same material was specified for the thermocouple plugs and nozzle body to reduce the risk of non-uniform thermal expansion.

The design of the fit began with the reamer that would ultimately ream the holes in the nozzle body. The reamer tolerance was given as +0.0002" -0.0000". This tolerance in conjunction with the highest tolerance that could be reasonably held on the 0.2500" plug shaft material of +0.0002" -0.0000" was used to create first set of nominal dimensions for a fit interference of 0.0005". The hole was nominally set to 0.2493" and the plugs to 0.2500". Despite these specified tolerances, the reamed hole diameter is not necessarily independent of the specific machine speeds, feed, and depth of cut, so some initial tests were performed to ensure that the holes could be reamed to within the above tolerances using a 0.2493" reamer. These tests were successful and indicated that the reamed holes were 0.2494".

Following these concluding tests, the plug design was formalized using the 0.500" nominal wall thickness. Proper location of the junction relative to the nozzle wall was extremely critical to the accuracy of the experimental results, so a locating feature was cut into the nozzle wall at each plug location. This 0.015" spot face served as a flat surface on the outside of the nozzle that could be used to stop the plug driver when the plug was pressed to the correct depth.

Table 3. Cal Poly 4:1 nozzle thermocouple plug axial locations.

Junction Number	Distance from Throat [in]	Nozzle Inside Radius [in]
1	2.000	1.320
2	1.500	1.181
3	1.000	1.043
4	0.625	0.939
5	0.250	0.846
6	0.000	0.826
7	-0.250	0.845
8	-0.500	0.905
9	-0.875	1.087
10	-1.375	1.437
11	-1.875	1.590
12	-2.375	1.601

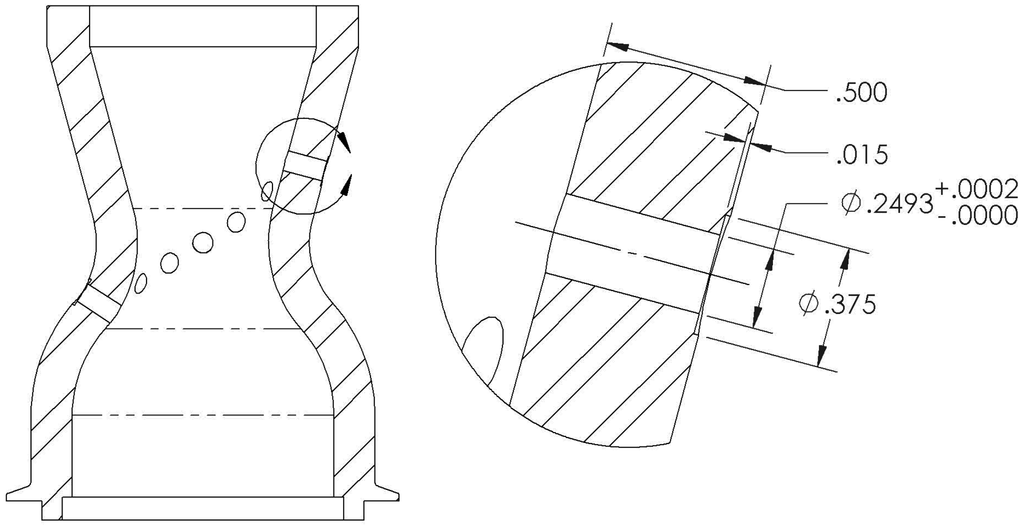

Figure 16. Cal Poly 4:1 nozzle section view and detail view of thermocouple plug interface. Dimensions are in inches.

Figure 17. Rendering of the Cal Poly 4:1 nozzle showing helically spaced thermocouple plug holes, Marman clamp geometry, and blast deflector mounting features.

To ensure proper placement of the holes and associated spot faces, all 12 holes were drilled in a single operation on a 5-axis milling machine using the setup pictured in Figure 18. Starting with a center dill, the hole was located. A 0.125" drill was used to pilot the hole before a 0.242" drill prepared the hole for the reamer. Before reaming, a 0.375" end mill cut the spot face. Last, the holes were reamed to final dimension using the 0.2493" reamer.

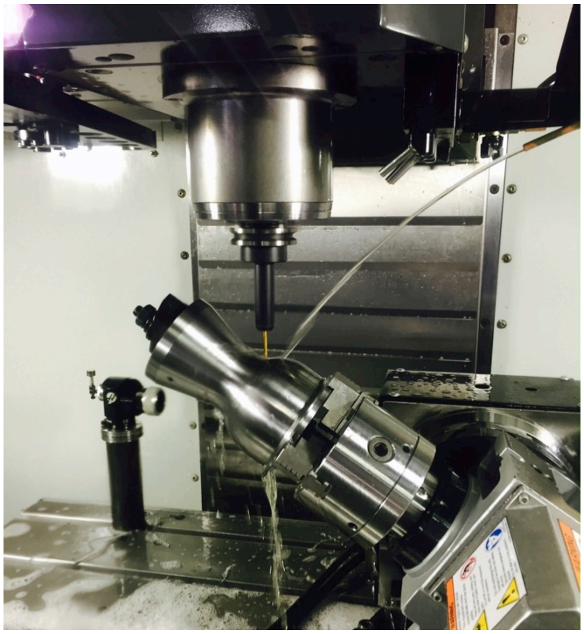

Figure 18. Pilot drilling thermocouple plug holes in the 4:1 nozzle on a 5-axis Haas VF-2.

A trunnion assembly, pictured in

Figure 19, was fabricated to hold the nozzle while a series of blocks were used to prop the assembly at different angles for pressing each plug. This system operated under the same principal as a traditional sine bar. When placed in a hydraulic press, a custom driver could be used to press each plug to the appropriate depth. This driver was designed to avoid damaging the thermocouple wires while still locating on the spot face.

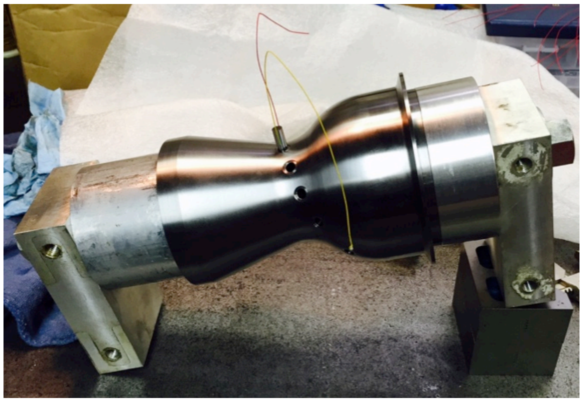

Figure 19. Trunnion assembly used to fixture nozzle during plug installation. Various blocks were used to prop the nozzle at each angle for installing the thermocouple plugs

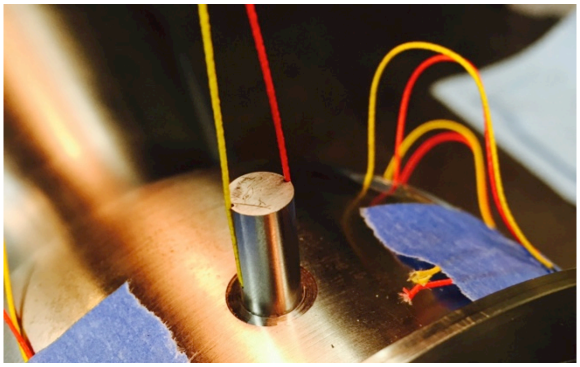

Figure 20. Thermocouple plug prior to installation into the nozzle body.

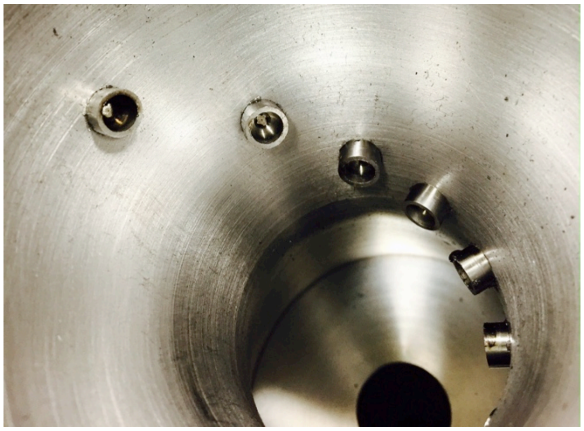

Figure 21. Nozzle inner bore following the installation of the 12 thermocouple plugs. The guide length and final thermocouple welds can be seen from the backside of the plugs.

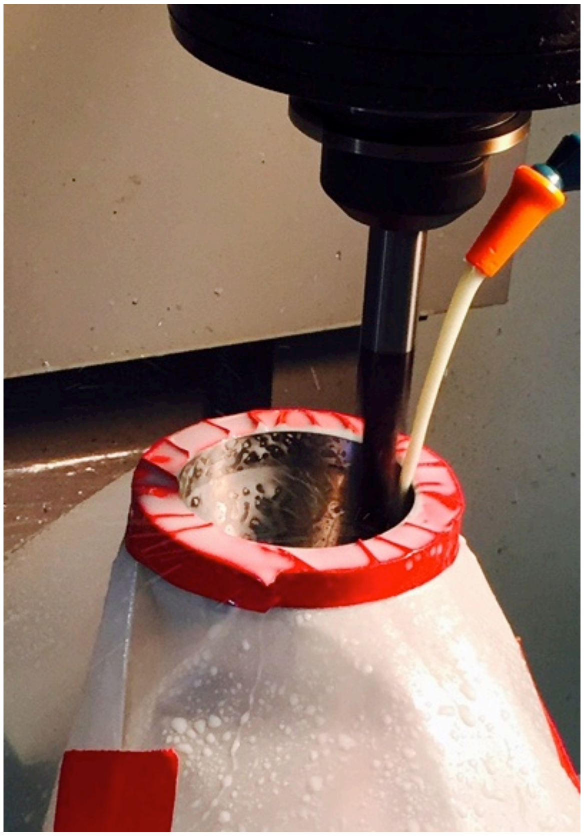

Figure 22. Removing the thermocouple plug guide length and machining the inner nozzle bore to the final profile on a Haas TM-1. The plastic shroud protects the nozzle body and thermocouple wires from exposure to the machine coolant.

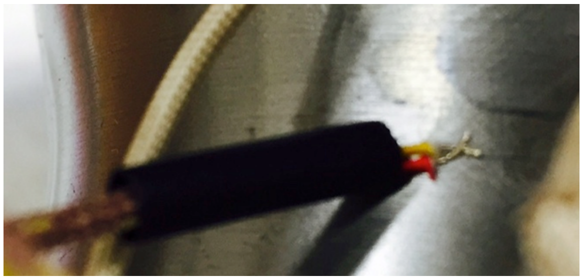

Figure 23. Outer surface junction formed using 24 gauge K-type thermocouple wires resistance welded to the outside of the nozzle body.

4. EXPERIMENTAL METHODS

4.1 Data Collection Technique

Experimental data were collected using an ADAM 5000TCP data acquisition system specially configured for the Cal Poly Hybrid test stand. The system is capable of reading numerous pressure transducers, thermocouples, and scales while controlling various other system setting including ignition flows and main oxidizer timing. Specifically for the testing conducted during this project, the system was configured to read oxidizer bottle supply weight, oxidizer supply pressure, precombustion chamber temperature, chamber pressure, and 18 K-type thermocouples distributed throughout the nozzle.

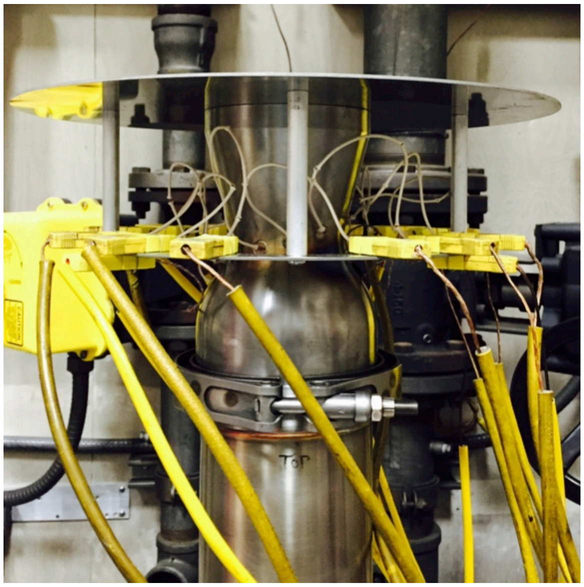

Figure 24. Complete Cal Poly 4:1 nozzle on the hybrid test stand with 18 thermocouple junctions wired to the data acquisition system.

All 18 thermocouple channels consist of a K-type thermocouple extension wire connected to a thermocouple amplifier, which reports an analog voltage signal to an analog input on the ADAM. Each of the channels was offset to read the correct temperature at 700°F using a transfer standard, and then the published amplifier gain was taken to be exact. The pressure transducer offsets and spans were set at 100 psig and then checked for linearity at 0 psig (open to the atmosphere) and at 50 psi. On channels where noise was apparent, the noise was considered acceptable if the reading was bounded by 3 DAC counts. For reference, the analog signals range from 0-10V and the ADAM uses 12-bit DACs producing integer values between 0 and 4095. The noise was crudely averaged for calibration purposes.

Due to the number of channels being recorded, the ADAM cooperatively multitasks between a series of user defined data acquisition tasks associated with various groups of channels. This results in data file associated with each task that has a unique time stamp. To produce data with a constant time step and time series that is consistent across all the data series recorded, the channels were resampled using a MATLAB script. This script uses linear interpolation between the data points recorded at approximately 20Hz to produce series with corresponding even time steps. The data could be further oversampled if subsequent analysis required.

Since the data collection system was not capable of reading 24 thermocouple channels, corresponding to 12 inner junctions and 12 outer junctions, 18 thermocouple junctions were sampled, corresponding to 12 inner junctions and 6 outer junctions. The 6 outer junctions were placed in axial alignment with every other inner junction. MATLAB script was then written to interpolate along the outer junctions to approximate the surface temperature corresponding to the other 6 inner junctions, which were not paired directly with an outer junction.

4.2 Data Processing Technique

With adjusted time series for each of the thermocouple channels, a master processing script was written to compute the experimental heat fluxes and film coefficients. The finite difference methods described in Reference 2 were implemented using the inner and outer temperature measurements as boundary conditions in a 1-D transient thermal analysis. The specific heat capacity and thermal conductivity of the steel nozzle body were assumed to be dependent on temperature according to the values in Table 4. These began with radial conduction in a hollow cylinder modeled by Eqn. 1.

$$\rho c_p \frac{\partial T}{\partial t} = \frac{\partial}{\partial r}\left(k \frac{\partial T}{\partial r}\right) + \frac{k}{r}\frac{\partial T}{\partial r} \qquad (Eqn. 1)$$

The finite difference approximations given by Eqn. 2 and Eqn. 3 were substituted into Eqn. 1 to develop Eqn. 4, which can be used to develop the time temperature history within the nozzle wall.

$$\frac{\partial T}{\partial t} \approx \frac{T_{i+1,j} - T_{i,j}}{\Delta t} \qquad (Eqn. 2)$$

$$\frac{\partial T}{\partial r} \approx \frac{T_{i,j+1} - T_{i,j-1}}{2\Delta r} \qquad (Eqn. 3)$$

$$T_{i+1,j} = T_{i,j} + \frac{\Delta t}{2(\Delta r)^2 (\rho c_p)_{i,j}}\Big[(k_{i,j+1} + k_{i,j})(T_{i,j+1} - T_{i,j}) - (k_{i,j} + k_{i,j-1})(T_{i,j} - T_{i,j-1}) + \frac{\Delta r k_{i,j}}{r_j}(T_{i,j+1} - T_{i,j-1})\Big] \qquad (Eqn. 4)$$

Table 4. Material properties from Reference 8 used to model the temperature dependence of the steel nozzle body.

Temperature [C]	Specific Heat [kJ/kg-K]	Thermal Conductivity [W/m-K]
100	0.486	51.1
200	0.520	49.0
400	0.599	42.7
600	0.749	35.6
800	0.950	26.0
1000	0.950	27.2

Evaluation of the difference equations produced a radial temperature distribution within the nozzle wall starting from the recessed thermocouple junction and extending to the outside wall. The temperature distribution history for the first station is displayed as a contour plot in Figure 25. The solution was checked for stability using Eqn. 5 and convergence using decreasing values for the special grid spacing since the temporal grid spacing was taken by the data sample rate.

$$\left(\frac{k}{\rho c_p}\right)_{max}\frac{\Delta t}{(\Delta r)^2}\le\frac{1}{2} \qquad (Eqn. 5)$$

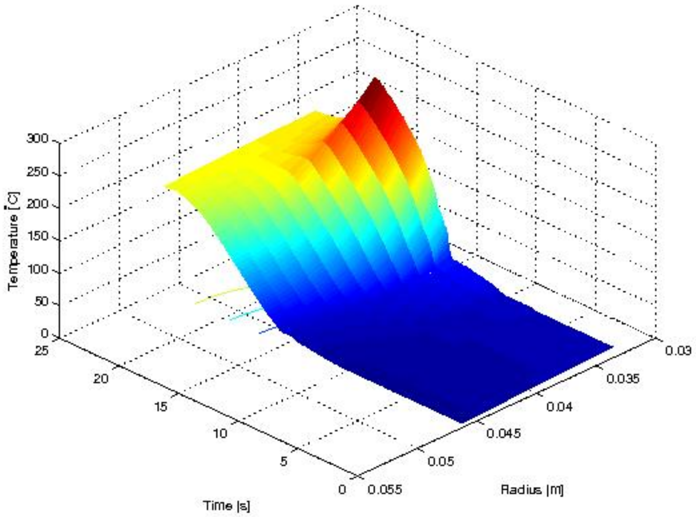

Figure 25. Contour plot showing the temperature distribution in the nozzle wall at station 1 throughout the duration of hot-fire #102.

To compute the wall heat flux, the temperature gradient at the inner nozzle wall is calculated from the internal temperature distribution. Rather than using the polynomial fit suggested in Reference 2, a sum of exponentials was fit to the temperature profile at each time step according to Eqn. 6. Data from one particular time step was curve fit and plot in Figure 26 and demonstrates the validity of the sum of exponential fit type. A brief survey of the known solutions to the 1-D transient conduction problem also indicates that this sum of exponentials function is similar to common solution forms. This curve could then be used to extrapolate the temperature gradient at the nozzle wall by evaluating Eqn. 7. With the temperature gradient, the heat flux or film coefficient could be calculated assuming the free stream temperature given by CEA[2]. Since CEA produces a series of results for each the nozzle entrance, throat, and exit, the values at the nozzle inlet were used for all analysis and assumed constant throughout the nozzle.

$$T(r) = ae^{br} + ce^{dr} \qquad (Eqn. 6)$$

$$\frac{dT}{dr} = abe^{br} + cde^{dr} \qquad (Eqn. 7)$$

$$q_f = -k\frac{dT}{dr} \qquad (Eqn. 8)$$

$$h_g = \frac{q_f}{T_o - T_w} \qquad (Eqn. 9)$$

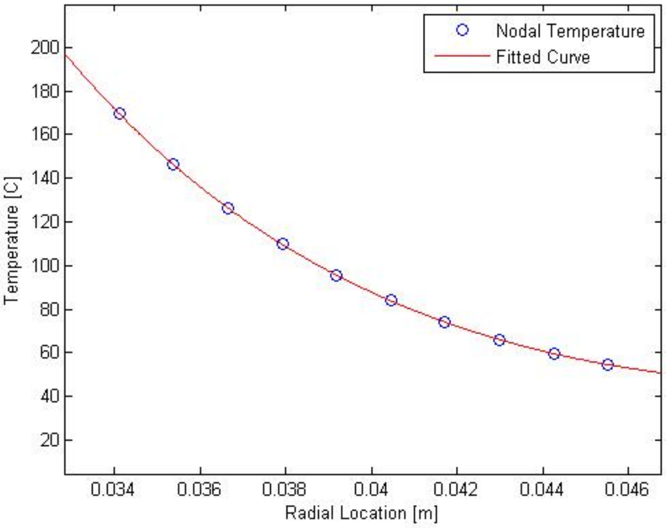

Figure 26. Nodal temperatures calculated using the finite difference method and subsequently curve fit using a sum of exponentials fit type.

---

[2] NASA Chemical Equilibrium Analysis can be downloaded or run online according to Reference 8

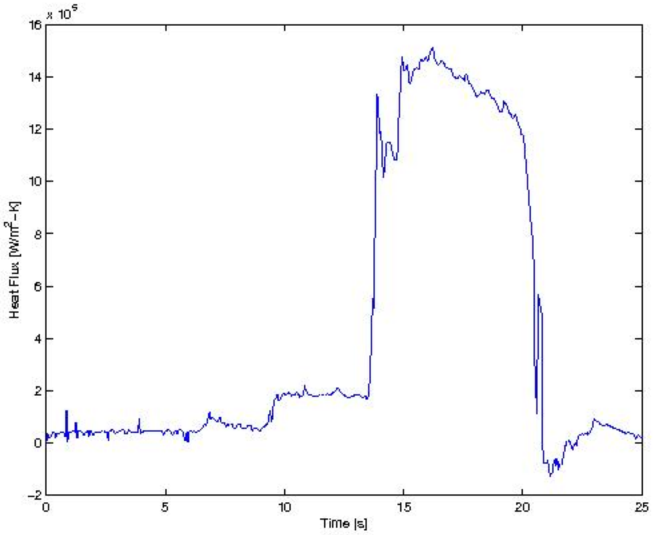

Figure 27. Wall heat flux calculated for each time step in hot-fire #102 at station 1 using Eqn. 8.

Generally, the published comparisons between measured and computed heat fluxes are shown for a constant wall temperature. Using a single wall temperature makes computing analytical heat fluxes simple for a particular geometry; however it complicates the data processing for an uncooled nozzle. Since the wall temperature at each station rises at a different rate, the heat flux is plotted when the wall temperature matches the selected wall temperature for comparison. Heat fluxes for a particular wall temperature are extracted from a curve fit of the computed heat flux versus wall temperature. Though Reference 2 demonstrates this approach works well for a liquid engine, less desirable results were initially observed on the Cal Poly hybrid motor. The surface temperatures at some locations indicated a linear relationship with the surface heat flux; however, many locations did not indicate a strong correlation. The large variations in measured surface temperatures and drifting chamber pressure, observed in the raw data, are consistent with the lack of correlation. These variations could be attributed to the rough starting nature of the hybrid motor, the grain/port configuration, the post combustion chamber length, or heavy sooting from the HTPB[3] fuel.

Rather than comparing the results at a constant wall temperature, the results are compared by averaging the measured heat flux and wall temperatures over a short 0.5s period during the steady combustion. These averaged wall temperatures are used in the Bartz equation solver to produce the heat fluxes given a non-uniform wall temperature. The heat fluxes and film coefficients can then be compared without extrapolating beyond the collected data.

In later tests, a 6" post combustion chamber length was added between the fuel grain and the nozzle. The post combustion chamber in conjunction with a cylindrical grain configuration provided a greater chance of developing an axisymmetric flow before entering the nozzle. The results of these tests were conducive to developing comparisons at constant wall temperature since the span of wall temperatures measured was smaller. Also, the chamber pressure maintained a steadier value in comparison with the decreasing value seen with the double-D grain configuration. Unfortunately, the rough starting nature created a long transient period of approximately 2s before useable steady combustion data was collected.

The final program used to process the measured wall temperatures was tested for convergence by varying the time and radial steps used in the finite difference equations. All the other processing techniques were held constant and the station 6 heat flux during hot-fire #104 was compared at a wall temperature of 1060°R. Although the data presented in Reference 2 indicates an extremely fine time step and radial increment are necessary to obtain accurate heat fluxes, reasonable convergence, less than 0.5%, is seen for rather large values. These observations can be attributed

---

[3] Hydroxyl-terminated polybutadiene is a rubber-like material when cured, commonly used as hybrid rocket fuel.

to the sum of exponentials fit that was used in place of the suggested polynomial fit. Ultimately, time increments equivalent to the average data collection increment of 0.050s produce reasonable results with radial increments that meet the stability criteria. Further reducing the increments shows that the solution converges below 0.1%; however, this requires interpolating along the data stream and introducing substantially smaller radial increments to maintain solution stability.

Table 5. Heat flux processing convergence study performed using data from hot-fire #104.

Δt [s]	Δr [inches]	Wall Temperature [°R]	Station 6 Heat Flux [W/m^2]	Stability Parameter $\left(\frac{k}{\rho c_p}\right)_{max} \frac{\Delta t}{(\Delta r)^2}$	Percent difference from converged
0.050	0.050	1060	2.0224×10^6	0.4147	0.4919%
0.025	0.050	1060	2.0216×10^6	0.2073	0.4522%
0.020	0.030	1060	2.0206×10^6	0.4608	0.4025%
0.010	0.025	1060	2.0109×10^6	0.3318	0.0795%
0.005	0.015	1060	2.0125×10^6	0.4608	-

5. EXPERIMENTAL TESTING AND RESULTS

Initial hot-fire testing of the 4:1 nozzle with 12 measurement stations was performed on the Cal Poly hybrid test stand using an annular PMMA fuel and nitrous oxide. Approximately 100 tests had successfully been completed on the hybrid test stand using PMMA or HTPB fuel with nitrous oxide. Various fuel grain port configurations had been tried including single circular ports, single annular ports, and double-D shaped ports. With the nitrous oxide bottles on the high side of the operating temperature range, oxidizer flow rates up to about 1.0 lbm/s could be achieved. The oxidizer flow rate is throttled by controlling the bottle temperature and the precombustion chamber injector configuration. The ignition is controlled manually by flowing a mixture of gaseous propane and oxygen to the precombustion chamber. These gasses are ignited by a continuously firing spark plug. Once the precombustion chamber temperature reaches an acceptable temperature (generally above 300°F) and a rich flame is observed at the nozzle exit, the main oxidizer is introduced and the ignition gas flows are shut off. After a preset burn duration, the main oxidizer is automatically shut off.

Unfortunately, the large throat area revealed that the previously used oxidizer flow rates were capable of extinguishing or flooding the grain. Extinguishment due to high oxidizer fluxes is typically referred to as grain flooding as described in Reference 12. Since the grain was flooded before steady combustion could be achieved, a slightly lower flow rate was tested; however, steady combustion was still not achieved. The flow rate could not be further lowered if choked flow was desired at the throat according to Eqn. 12. Flooding limit data, fuel regression correlations, and transient observations were compared to those described in Reference 10, Reference 11, and Reference 12.

$$\dot{m} = \frac{g_o p_1 A_t}{c^*} \qquad (Eqn.\,10)$$

$$\dot{m} = \dot{m}_o + \dot{m}_f = \dot{m}_f(1 + R) \qquad (Eqn.\,11)$$

$$\frac{p_1}{p_o} = \left(\frac{2}{\gamma+1}\right)^{\frac{\gamma}{\gamma-1}} \qquad (Eqn. 12)$$

Table 6. Summary of tests conducted using the Cal Poly 4:1 nozzle.

Test Number	Injector Count	Injector Diameter [in]	N_2O Bottle Pressure [psi]	Fuel Configuration	Results
98	3	0.073	704.3	Annular PMMA	Grain flooded
99	6	0.025	785.1	Annular PMMA	Grain flooded
100	6	0.025	678.9	Annular HTPB	No choked flow
101	6	0.036	687.7	Annular HTPB	No choked flow
102	8	OPEN	799.3	Double-D HTPB	Choked flow
104	12	OPEN	670.6	Cylindrical HTPB	Choked flow

$$G_o = \frac{\dot{m}_o}{A_p} \qquad (Eqn. 13)$$

$$\dot{r} = aG_o^n \qquad (Eqn. 14)$$

With limited success using PMMA fuel, HTPB was selected due to its significantly lower activation energy and much higher flooding limit. Again, an annular HTPB fuel grain was tested using oxidizer flow rates expected to choke the flow at the nozzle throat. After configuring the injector plate, a short cold flow of oxidizer was performed to estimate the flow rate during the hot-fire. This observed flow rate was then used to determine the nozzle pressure ratio expected using published regression rate correlations for HTPB fuel with nitrous oxidizer. With plenty of margin above the critical nozzle pressure ratio, the tests were performed. Though these tests did not produce choked flow, they revealed that the published regression rate correlations, given in the form of Eqn. 13 and Eqn. 14, were not valid for the particular operating conditions. Instead of running extremely rich as predicted, the motor was running much leaner. This can be directly associated with the grain not regressing as quickly as the published correlations indicated.

5.1 Hot-fire #102

To better ensure choked flow, a double-D grain was selected and the mass flow rate was increased to the maximum by opening all available injectors. This test successfully choked the flow and produced temperature measurements, plotted in Figure 28 and Figure 29, that could be processed to compute experimental heat flux values for each station.

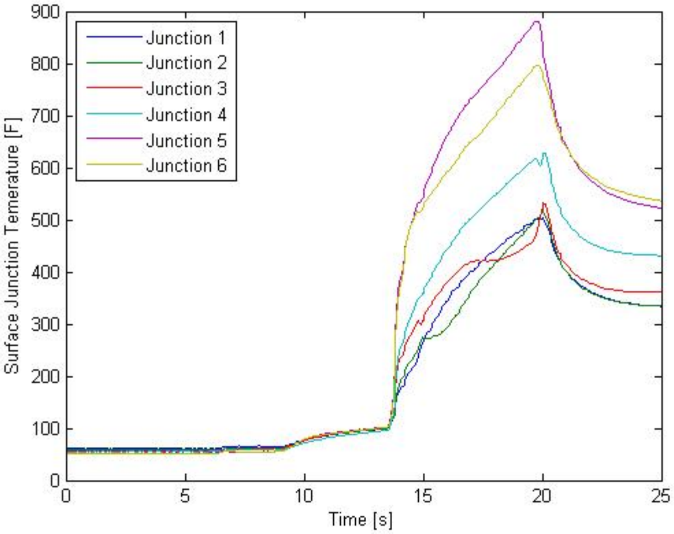

Figure 28. Raw junction temperatures 1-6 measured in hot-fire #102.

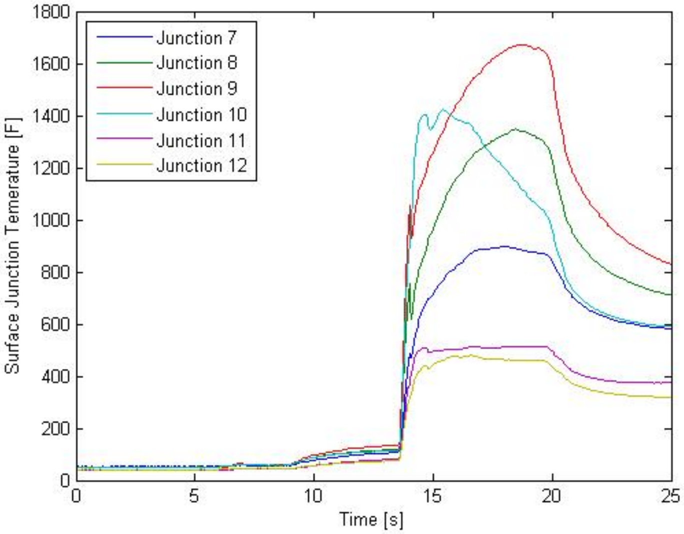

Figure 29. Raw junction temperatures 7-12 measured in hot-fire #102.

These results from hot-fire #102 are summarized in Figure 30 by comparing the film coefficients calculated from the experimental data and those predicted by the Bartz model. Figure 31 includes the corresponding experimental error at each station. Noticeably higher experimental errors are reported for the stations positioned directly above a port of the double-D grain. Without a substantial flow conditioning section before the nozzle, the combustion gasses exiting the fuel grain ports impinge directly on the nozzle surface and produce much higher surface temperatures than in areas where more mixing has occurred.

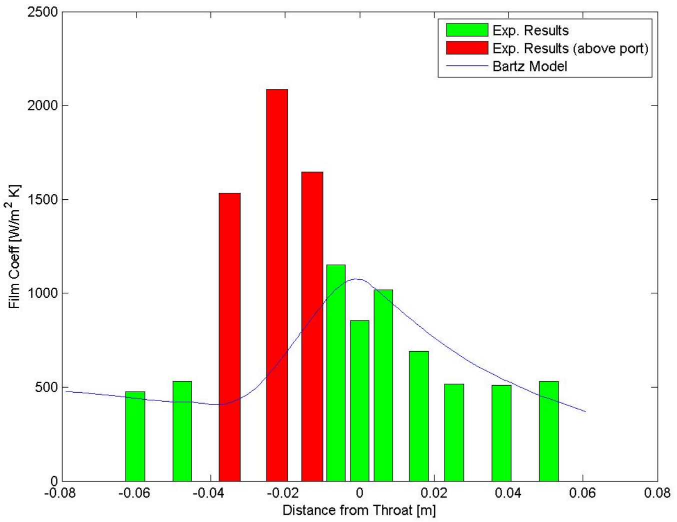

Figure 30. A summary of the results from hot-fire #102 showing the predicted and experimental film coefficients.

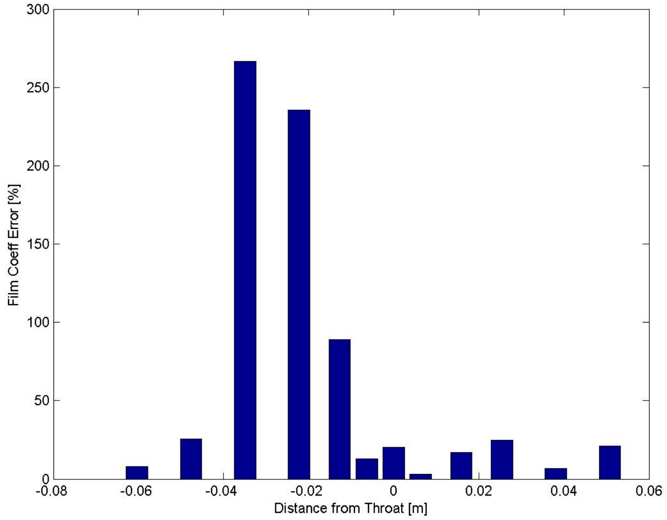

Figure 31. Error in the calculated experimental film coefficient. Note that all stations not directly above a port of the grain yield less than 30% error.

The errors due to an asymmetric (theta-wise) fuel grain may also be magnified by the locations of the outer junctions. Since an axisymmetric burning pattern was assumed, the outer surface junctions were placed in convenient locations for wiring and welding rather than directly outside their respective inner junction. However, when the nozzle was heated unevenly, the wall temperature gradient cannot be accurately computed by thermocouples at different theta-wise locations.

5.2 Hot-fire #104

In later tests, the 6" post combustion chamber was installed in conjunction with a cylindrical grain. These improvements produced a more symmetric flow regime, which resulted in experimental data that could be processed and compared at a constant wall temperature. The linearly increasing temperatures, plotted in Figure 32 and Figure 33, indicate a considerable duration of steady chamber pressure and imply that the heat flux should be linearly related to the wall temperature.

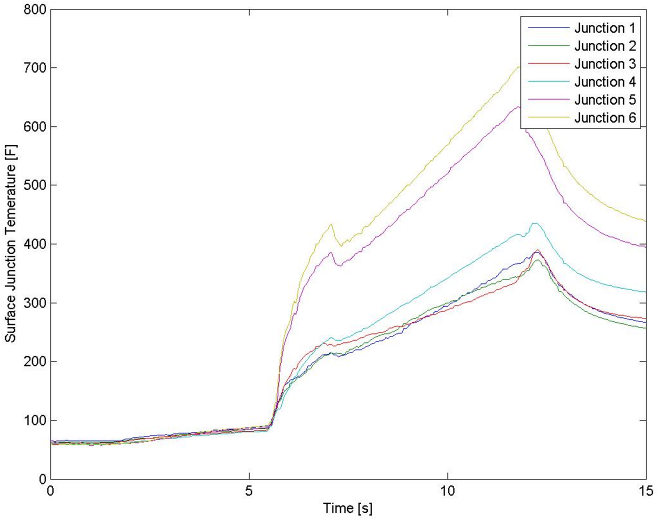

Figure 32. Temperature time history plot for surface thermocouples 1 through 6 during hot-fire #104.

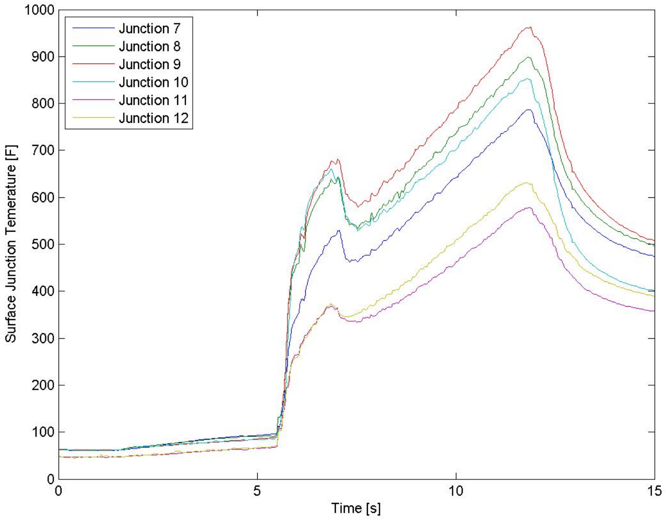

Figure 33. Temperature time history plot for surface thermocouples 7 through 12 during hot-fire #104.

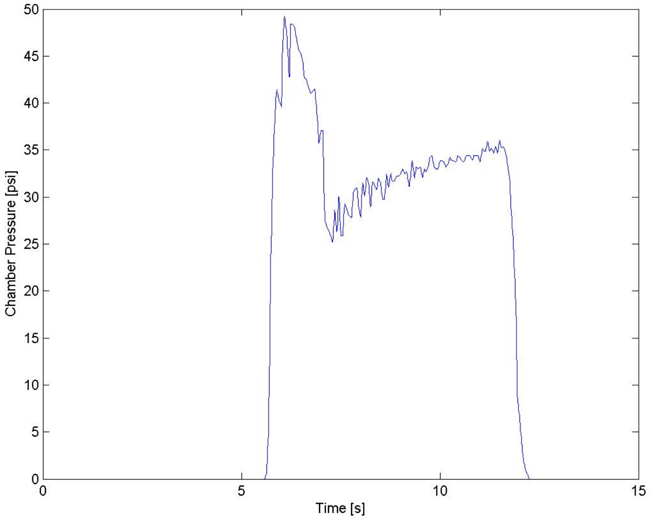

Figure 34. Pressure time plot for hot-fire #104 showing initial instability.

Despite an overall improvement in the data, the rough starting nature of the hybrid motor placed a significant heat load on the nozzle before steady combustion data could be collected. The temperature time histories show this high heat load in the 5s to 7s period when the wall temperature rapidly increased. Although the transient temperature response settles out after 7s, the converging section of the nozzle remains at substantially higher temperature as seen in Figure 33.

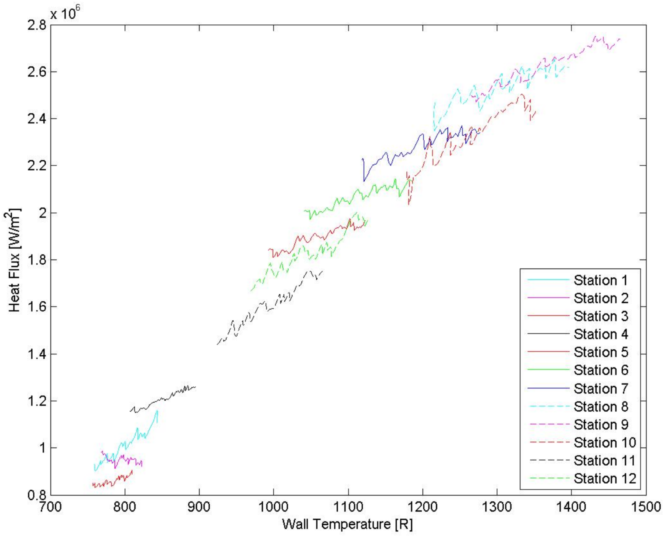

Figure 35. Computed wall heat fluxes plotted against the extrapolated wall temperature during the steady part of hot-fire #104.

Continuing to process the raw temperature data produces the expected a strong linear relationship between wall temperature and surface heat flux summarized in Figure 35. Unfortunately, the large variation in wall temperature axially makes selecting a single wall temperature for comparison difficult. Representative temperatures could be selected for each the converging and diverging sections that indicated excellent agreement with the Bartz equations. Figure 36 and Figure 37 show agreement between the Bartz model and experimental results at 750 °R. The experimental results are consistently higher than the Bartz model when reasonable agreement is observed; however, the throat region of the nozzle reports consistently lower film coefficient. Also, Reference 2 indicates that the heat flux decreased with increasing wall temperature, which is consistent with a decreasing driving potential. However, the data presented in the data presented in Figure 35 consistently indicate heat flux increases with wall temperature, which implies a true steady combustion may not be present despite the rather steady chamber pressure.

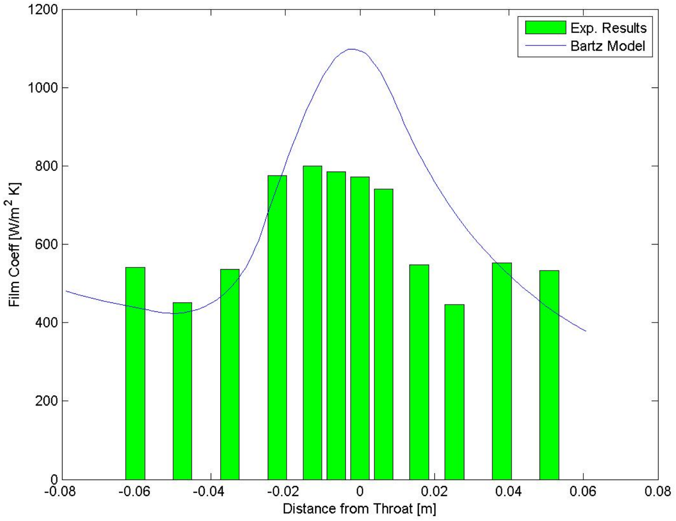

Figure 36. Comparison between computed experimental film coefficients and analytical Bartz model for a 750 °R wall temperature.

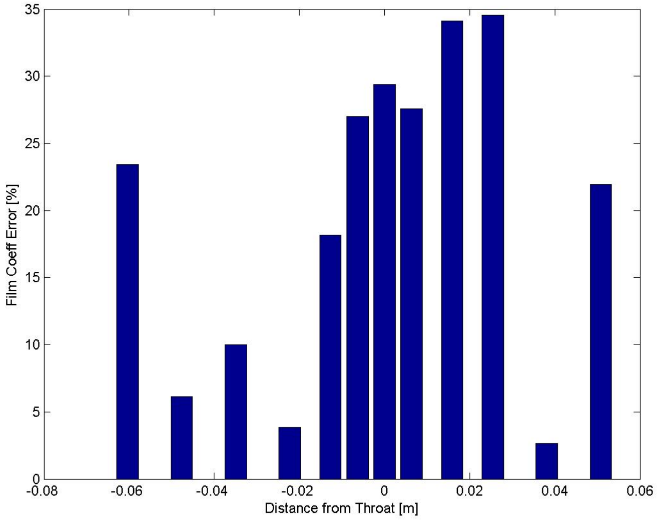

Figure 37. Error between computed experimental film coefficient and analytical Bartz model for a 750 °R wall temperature.

When the wall temperature used for comparison is increased to 1060 °R, excellent agreement is seen in the throat region and diverging section. Agreement at this temperature is not surprising after reviewing the distribution in Figure 35 since 1060 °R represents a reasonable middle ground that minimized extrapolation from the experimental results. Although the Bartz model does not agree with the experimental results in the converging section, the trends do agree. At the entrance, the film coefficient drops to a local minimum before rising to its peak at the throat. As suggested in Reference 1, the initial conditions used in the Bartz model can be set to match the measured film coefficient; however after seeing agreement at lower temperatures and in the diverging section, changing the initial conditions to produce better agreement in Figure 38 was not considered fair practice. Thought the initial conditions have limited influence downstream of the throat, changes to the initial conditions increase the error reported in the diverging section of the nozzle.

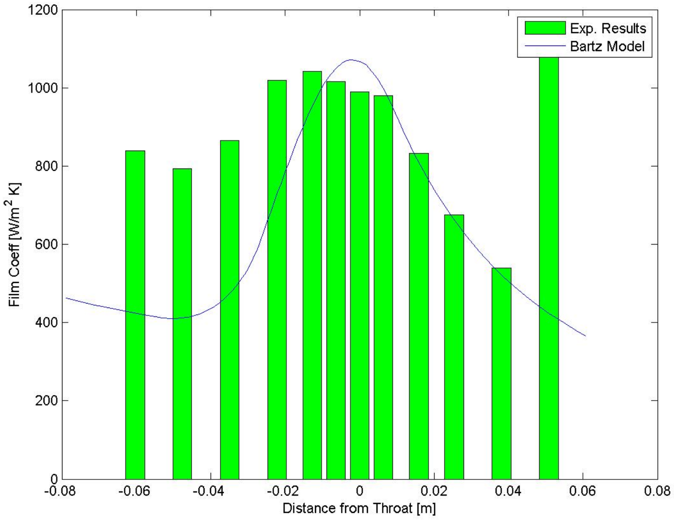

Figure 38. Comparison between computed experimental film coefficients and analytical Bartz model for a 1060 °R wall temperature.

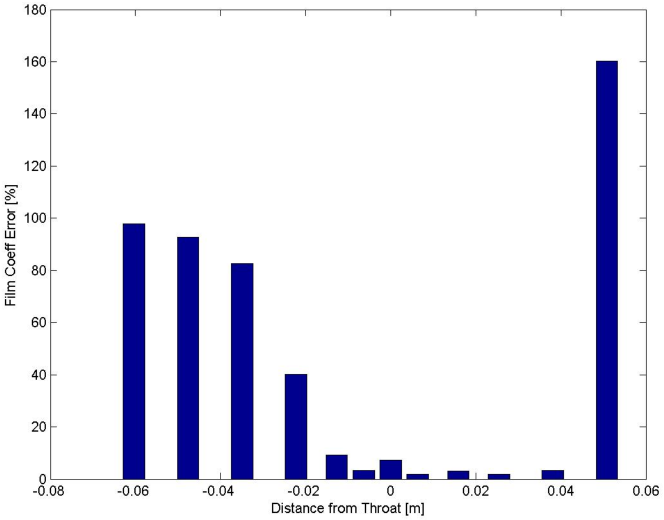

Figure 39. Error between computed experimental film coefficient and analytical Bartz model for a 1060 °R wall temperature.

Despite all stations demonstrating agreement with the model for a representative wall temperature, agreement is not observed for a single wall temperature. This discrepancy is attributed to the large heat flux imposed on the converging section of the nozzle during the transient period. Following the transient period, there is already a large temperature gradient in the nozzle both axially and radially; thus, the steady combustion heat fluxes reported in Figure 35 are separated by substantially different wall temperature ranges.

Although changing the initial conditions does not seem logical, the Bartz model can be configured to develop the boundary layer from approximately zero thickness. Following this process and assuming a unity shape factor produces a sharp peak in heat flux near the start of the nozzle where the boundary layer assumptions are less valid. Ignoring this portion of the data is common practice, as the data for the developed boundary layer is considered accurate. Figure 40 and Figure 41 compare the Bartz model to the experimental film coefficient at 960 °R assuming the boundary develops from the start of the nozzle assembly. This assumption produces a more uniform error distribution; however, in the converging section, the model under predicts and in the diverging section, the model tends to over predict the film coefficient. The large discrepancy seen as the exit of the nozzle is not consistent with any of the proposed theories, but could be caused by nozzle exit effects.

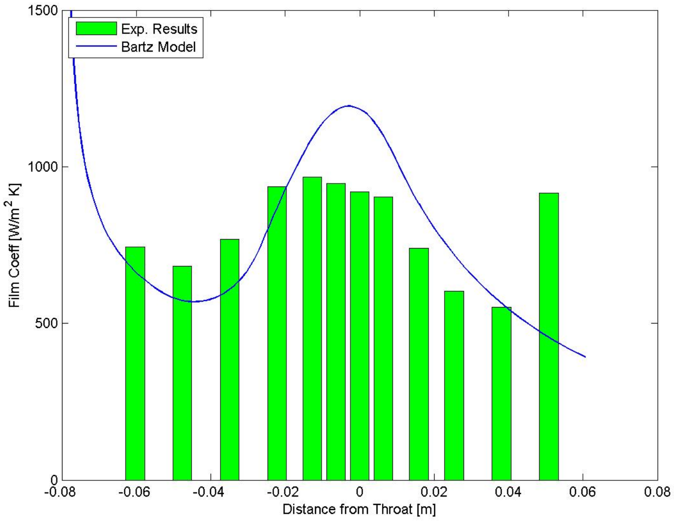

Figure 40. Comparison between computed experimental film coefficients and analytical Bartz model for a 960 °R wall temperature with the solver developed boundary layer.

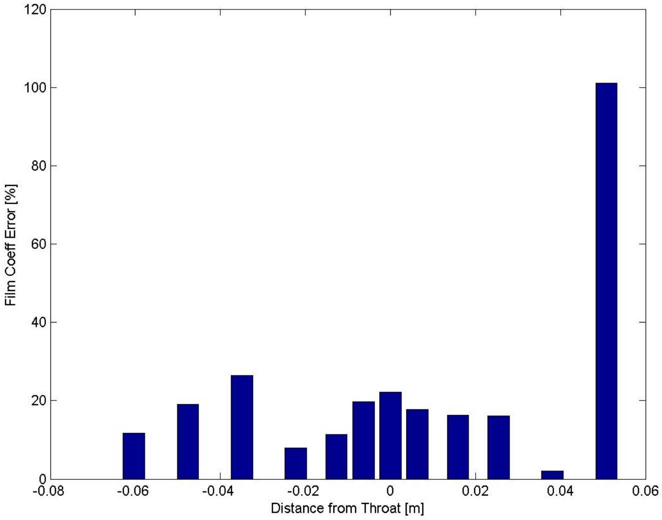

Figure 41. Error between computed experimental film coefficient and analytical Bartz model for a 960 °R wall temperature with a solver developed boundary layer.

When agreement is seen between the experimental results and Bartz model, the model tends to under predict the film coefficient, which implies other effects not included in the Bartz model likely contribute to the wall flux. These may include transient, radiation, sooting, varying chamber pressure, and varying specific heats. A more complicated analytical model or cleaner burning fuel may be able to compensate for these discrepancies. Although the Bartz model is capable of handling variations in wall temperature, it provides a steady state solution, which may be less accurate when compared to data collected in a transient environment. In a situation where the nozzle wall temperatures were heating uniformly, or at least from a similar starting point, this assumption may be more valid; however, when the all the data taken with large axial variations in temperature, the transient nature of the boundary layer may play a larger role.

5.3 Error Analysis

Throughout the experimental setup and data processing, there are numerous uncertainties and errors from both manufactured components and computed values. The largest of these errors will be discussed and their influence on the final computed heat flux will be investigated. The summary in Table 7 contains the major sources of error identified in the experimental and computational processes that ultimately sum to an experimental error of ± 5.2% of the computed heat flux.

Table 7. Summary of errors in the experimental fabrication, data collection, and data processing.

Source of Error	Estimated Error	Effect on Computed Heat Flux
Inner junction location relative to driven end of plug	± 0.0005"	-
Inner nozzle wall surface location	± 0.0010"	-
Spot face location relative to inner nozzle wall	± 0.0020"	-
Assumed total junction location error	± 0.0023"	± 0.5%
Thermocouple amplifier and reading	± 7 °F	± 0.6%.
Finite difference method and extrapolation to inner surface	-	± 4.0%
Temporal interpolation of data	-	± 1.0%
Inner junction temperature	>1% of recorded temperature	± 0.6%.
Outer junction axial interpolation	± 17 °F	± 3.0%
Total Error	**-**	**± 5.2%**

The inner junction location relative to the driven end of the plug is crucial to the final junction location since this end of the plug is driven until flush with the outer nozzle wall. To minimize this error, all critical features of the thermocouple plugs were machined from this end in a single setup on a 5-axis milling machine. The error is reported as ±0.0005" which is the setup tolerance of the machine. Measurements taken before machining indicate that the setup was within this tolerance. Also, the guide length of the thermocouple plugs was clearly cut entirely around the plug stock at a depth of 0.0005" implying that the setup was likely within 0.0005"; otherwise, features of this size would appear asymmetric. The inner nozzle wall surface location is assumed to be with ±0.0010" of the target location since the nozzle was indicated straight and on center within 0.0005". The remaining tolerance is added to account for tool deflection, surface finish, and machine tolerance. The spot face locations relative to nozzle wall is assumed to be within ±0.0020". Although the nozzle was indicated within 0.0005" when placed in the milling machine, the nozzle was far from the pivoting axes, which allowed any deflection or slight misalignment of the rotary unity to be magnified. Combining the above tolerances indicates that the junction locations are likely located within ±0.0023", which is significantly more accurate than the ±0.0040" assumed by Reference 2.

To study the effects of junction location error, the heat flux was recalculated assuming the junction was located on either edge of the specified tolerance. These studies simulated the sensitivity to the computed heat flux assuming that the junction location was updated with a precise location within the specified tolerance. The results of these studies, reported in Table 8, indicate that the error caused by junction location can reasonably the considered ±0.5%.

Table 8. Sensitivity of computed heat flux to changes in the junction location within the manufacturing tolerances computed using $\Delta r = 0.050"$ and $\Delta t = 0.050s$.

Thermocouple Junction Radial Setback [inches]	**Station 6 Computed Heat Flux [W/m^2]**	**Percent Variation From Nominal Setback**
0.0226 (nominal)	2.0224×10^6	-
0.0226 + 0.0023	2.0307×10^6	+0.4104%
0.0226 – 0.0023	2.0143×10^6	-0.4005%

The thermocouple reading error is largely due to drift and nonlinearity observed in the thermocouple amplifier boards. Using a transfer standard, the data collection system was checked across the range of operating temperatures. Variations up to ±7°F were observed; however, considering the temperatures recorded ranged from 50°F to 1700°F, this variation was not concerning. The influence of this variation on the computed heat flux was studied in a similar fashion to the thermocouple setback. The variation is conservatively rounded up to ± 0.6%.

Table 9. Sensitivity of computed heat flux to changes in the reported thermocouple temperature computed using $\Delta r = 0.050"$ and $\Delta t = 0.050s$.

Thermocouple Junction Reading	**Station 6 Computed Heat Flux [W/m^2]**	**Percent Variation**
+ 0 °F (as recorded)	2.0224×10^6	-
+ 7 °F	2.0122×10^6	-0.5043%
- 7 °F	2.0328×10^6	+0.5142%

The finite difference method introduces a particular uncertainty since discrete values for the radial and temporal step size must be chosen. Also, the resulting radial temperature distributions must be used to determine the temperature gradient at the inner nozzle wall. The uncertainty in the finite difference extrapolation taken from Reference 2, where a comprehensive analysis was conducted to determine any errors introduces from the curve fitting or numerical techniques. However, since a sum of exponentials curve fit is employed rather than the suggested polynomial, the lower error bound of ±4% is chosen. The temporal interpolation of data error also taken from Reference 2 as ±1%.

The inner junction temperature error is taken from the finite element analysis presented for the new thermocouple plug design. The finite element analysis indicates the plug design may influence the measurement on the order of 1%, which is comparable to the thermocouple reading error. Thus, the influence on the computed heat flux is assumed to also be ± 0.6%.

The outer junction axial interpolation error is introduced since only 6 outer junction temperatures could be measured. An interpolation was performed to produce values corresponding to all 12 inner surface junctions. The error is taken as a quarter of the largest average difference between successive outer junctions during part of the data analyzed. The largest average difference between successive outer junctions for hot-fire #104 was 67.2 °F, so the outer junction interpolation error was taken to be ± 17 °F. The influence of this variation on the computed heat flux was studied in a similar fashion to the thermocouple setback. The variation is conservatively rounded up to ± 3%.

Table 10. Sensitivity of computed heat flux to changes in the reported outer thermocouple temperature computed using $\Delta r = 0.050"$ and $\Delta t = 0.050s$.

Outer Thermocouple Junction Interpolation	**Station 6 Computed Heat Flux [W/m^2]**	**Percent Variation**
+ 0 °F (as interpolated)	2.0224×10^6	-
+ 17 °F	1.9714×10^6	-2.5217%
- 17 °F	2.0757×10^6	+2.6354%

6. ANALYTICAL MODELING: Bartz Model for the Turbulent Boundary Layer

Rather than using the common short form of the Bartz equation given in Reference 13 or Reference 10, a solver was developed in MATLAB similar to the one described in Reference 1. Using the methods in Reference 1, the integral form of the momentum and energy equations is integrated along the axis of the nozzle; the code is available in Appendix A. This solver was validated using the test case presented and then adapted to the nozzle geometry and combustion products used in the experimental tests. Figure 42 contains traces of the computed heat flux using the MATLAB code in Appendix A overlaid with the test case data presented in Reference 1.

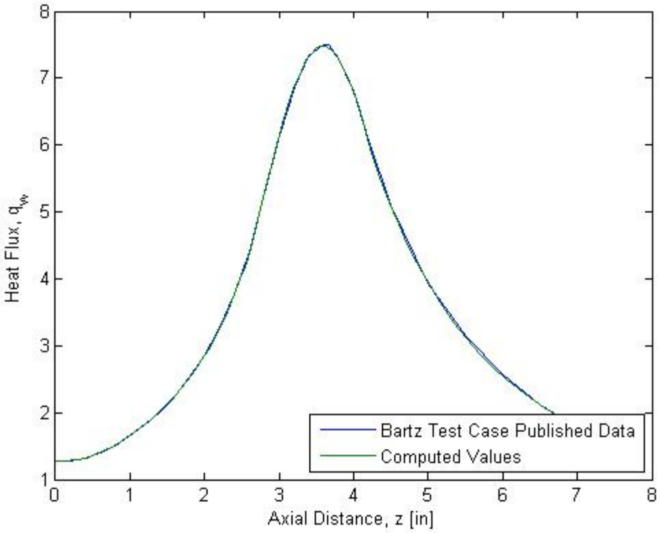

Figure 42. One of several plots used to validate the Bartz solver for the test case presented in Reference 1.

7. ANALYTICAL MODELING: FLUENT Validation for Predicting Heat Fluxes

Throughout this validation, the well known and experimentally validated Bartz equations and methods will be compared with results of FLUENT simulations. A simultaneous momentum and energy equation solver, built in MATLAB according to process outlined in Reference 1, will be used to generate and compile data for suggested test cases. Data presented in Reference 1 is summarized for two experimental tests in Figure 43 below and demonstrates excellent agreement with the simulation results.

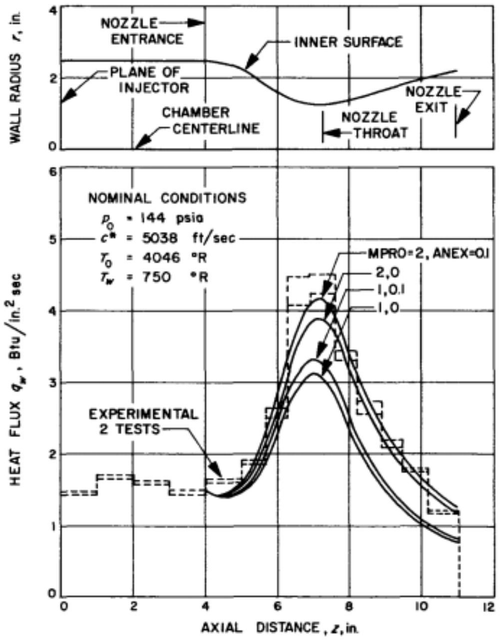

Figure 43. Comparison of simulation and experimental results from Reference 1.

Rather than continuing to superimpose raw experimental data, this validation will continue by comparing the results of the previously described simulation with the FLUENT results.

7.1 Purpose

The purpose of this validation is to confirm that FLUENT accurately models the surface heat transfer coefficients in axi-symmetric nozzles. Since chocked flow is expected at the throat, the flow is transonic in the domain and a compressible model must be incorporated. Commonly, this case is simplified to inviscid flow since the boundary layer is extremely thin; however, considering surface heat transfer requires that the boundary layer be modeled in detail. Various methods were explored for achieving accuracy close to the wall including various wall functions and near wall treatments.

7.2 Problem Description

Reviewing Reference 1 provides a method for calculating the surface heat fluxes by integrating the momentum and energy boundary layer equations for a 1-D nozzle flow. The paper also provides a sample solution for a generic converging-diverging nozzle. A similar solver has been developed in MATLAB and validated using these results; thus, any nozzle geometry can be computed. However, throughout this validation the test case geometry provided in Reference 1 will be used. The nozzle has an entrance diameter of 5 inches, a length of 7.5 inches, and a contraction ratio of 8:1. This geometry is coupled with a straight entrance section both in the MATLAB simulation and the FLUENT model. An entrance length of 6.25 inches has been selected since these values agree with the raw output data provided in Reference 1. These data are imported to ICEM using formatted XY point data and connected with splines.

The properties of the fluid are again modeled according to Reference 1. The fluid is assumed to be the completely combusted products of N_2O_4-hydrozene. The fluid is considered a compressible ideal gas with constant specific heat of 0.567 Btu/lb-°R. Both viscosity and conductivity are modeled as functions of temperature. The built in power law relationship is used for viscosity; however, conductivity follows a constant Prandlt number of 0.83 and requires a user defined function since the form of the equation is not natively available.

$$\frac{\mu}{\mu_0} = \left[\frac{T}{T_{0i}}\right]^n \qquad (Eqn. 15)$$

$$\mathrm{Pr} = \frac{c_p \mu}{k} \qquad (Eqn. 16)$$

Rearranging,

$$k = \frac{c_p \mu_0}{\Pr}\left[\frac{T}{T_{0i}}\right]^n \qquad (Eqn. 17)$$

Note the constants are taken form Reference 1 as μ_0 = 4.186e-5 lb-s/ft^2, T_0 = 4500 °R, and n = 0.65. Finally, the molecular weight is specified. Since the molecular weight depends on the nature of the combusting gasses, a NASA Chemical Equilibrium Analysis program was run to determine the resulting molecular weight for the motor assuming an oxidizer to fuel ratio of 2, which resulted in a value of 23.199 lb/lbmol. See Reference 8 for the online version of the CEA program where the results can be obtained.

Once grid artifacts have been removed with a grid study, the chamber pressure was varied between 100 psi, 200 psi, and 300 psi to model different nozzle operating points. All other boundary conditions and fluid properties were assumed to remain constant.

A 2-D axi-symmetric model is implemented with axis boundary conditions along the x-axis, pressure inlet/outlet at either end, and wall boundary conditions along the nozzle contour. The wall boundary conditions were set to the temperature specified in Reference 1 of 1125 °R. The exit plane pressure outlet was set to atmospheric pressure and the inlet was set to the particular chamber pressure. The inlet temperature was set to the combustion temperature of 4500 °R. Since no backflow was expected at the inlet or outlet, these conditions were not found to be significant. However, since the combustion is strongly turbulent, the default fully turbulent parameters for turbulent kinetic energy and epsilon were used.

7.3 Grid

Initial familiarity with the problem was developed through an inviscid calculation. A coarse, unbiased grid was created for the geometry described above. The results of this calculation agreed with the free-stream solution.

In expectation of the boundary layer appearing along the wall sections, the grid was heavily biased in this direction. A geometric growth rate was used to blend the grid towards the center of the nozzle. Reviewing the FLUENT documentation indicated that grids should not start with elements in the buffer region, so to increase computational efficiency, the first element was placed in the log layer and enhanced wall functions were used to extrapolate to the wall boundary. Alternatively, elements could be placed in the viscous sublayer and used to capture the complete law of the wall behavior. The law of the wall region is mapped using the dimensionless parameter y^+ given by the equation:

$$y^+ = y\sqrt{\frac{2}{c_f}}\frac{\mu}{\rho U} \qquad (Eqn.\, 18)$$

The form of the above equation has been taken from the FLUENT documentation on "Turbulence and Near-Wall Modeling"; however, it has been modified to include the flow density, ϱU, rather than the kinematic viscosity since the simulation in Reference 1 is configured to output flow density. With flow density as an output from the validated simulation, these results can be used to compute the compute the locations of the first node based on desired y+ values.

The results of these computations are summarized in Figure 7.1 below. A value of 0.001 was selected initially to maintain y+ on the order of 30 throughout the nozzle. It is worth noting that the radial distance associated with a particular value of y+ changes drastically depending on the axial location due to changing flow density and viscosity. All of the grids computed yielded at least 15 elements through the boundary layer which falls within the recommended 10-20 elements. A geometric bunching law was used to avoid excessive grid density in the free stream while maintaining at plenty of elements in the boundary layer. The resemblance to the system layout in Figure 43 can easily be seen.

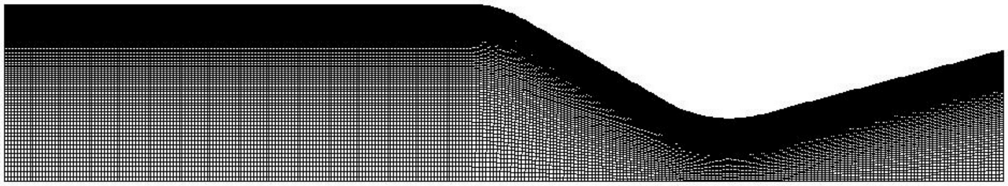

Figure 44. Generic grid example showing entrance length with mesh heavily biased towards the boundary layer.

For simplicity during grid generation and updating, the nozzle was blocked into three sections along the axis: the first straight section, the converging section, and the diverging sections. Parallel edge copying allowed all the vertical edges to be meshed with the previously discussed bunching laws and a constant number of uniformly spaced element were placed along each of the outer wall curves.

7.4 Case Setup

Throughout this validation, all fluid properties will remain constant and the chamber pressure will be varied between 100 psi, 200 psi, and 300 psi. Each of these are realistic operating pressures for this nozzle as the produce chocked flow in the throat. The nature of operating this nozzle generally results in different fluid properties at each pressure; however, all properties, particularly molecular weight and combustion temperature, were held constant.

7.5 Calculation

In the general setup, the density-based solver was selected because a transonic flow was expected. Axisymmetric was also selected in the 2-D space because the nozzle can easily be simplified to an axisymmetric model. In the models setup, the energy equation was enables since surface heat transfer coefficients were the main variable of interest. For the viscous model, realizable k-epsilon with enhanced wall treatment was determined to be best suited for the problem; however, other wall functions and the k-omega models were used with reasonable results. All other parameters remained default.

Reference values were computed from the fluid region; however, the values of pressure and velocity represented the expected magnitudes at the inlet. The implicit solver with Roe-FDS was used in conjunction with Green-Gauss node based gradients and second order upwinding for all parameters. Default relaxation factors were used for all parameters. The absolute normalized residual criteria was set to 1e-6 for all parameters. The solution was initialized with the same values described for the reference values relative to the cell zone. Solution steering was used with full multi-grid for transonic flow. First to higher order blending was disabled, or set to zero. After running the calculation a few times, it was found that the stage 1 iterations could be reduced to 20 and the Courant number, a dimensionless time step, was given a maximum values of 1000. Despite this increase, the Courant number rarely exceeded the default maximum of 200. For the grids with finer elements, the number of cycles per multi-grid level was increased to produce more accurate solution steering. With these almost default settings in place, the solution was found to converge in less than 400 iterations on all the grids described.

Various solution setups were tested as part of this validation; particularly, grid density surrounding the wall region was studied in conjunction with various wall functions. Ultimately, with the increased functionality available through enhanced wall functions, it is recommended to create grids with the first node with y^+ between 30 and 300. Values in this range keep the nodes outside the inner and buffer regions allowing the wall functions to represent the flow back to the wall. It is important to note that for a given first node spacing along the nozzle, the associated value of y^+ varies. This variation can be attributed to changes in the flow density as the fluid accelerates in the nozzle.

Using the results from the 1-D simulation according to Reference 1, these variations were accounted for while determining the first node location. Knowing that y^+ can safely exceed 30, a baseline series of locations were computed along the nozzle. These are showing in Figure 45. Based on this graph, three initial spacing of 0.001", 0.003", and 0.005" were selected. To compare these with the recommendations in the FLUENT documentation resulting values of y^+ were calculated along the axis of the nozzle. These results are plotted in Figure 46.

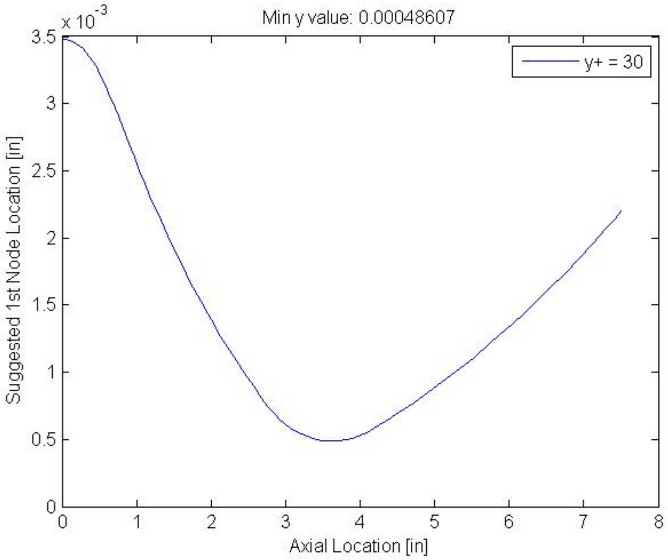

Figure 45. Suggested 1st node locations based on a lower bounded y^+ of 30. Note that the values vary significantly along the nozzle geometry. Since larger values are acceptable, a first node location anywhere in the presented range should be acceptable.

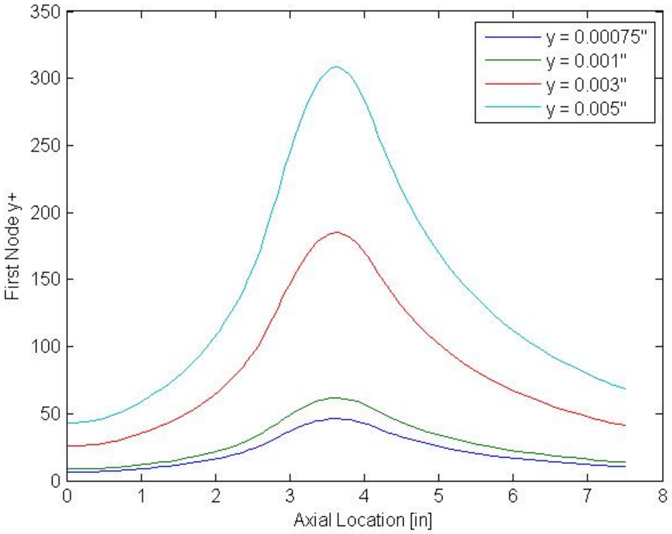

Figure 46. Computed values of y^+ based on constant first node spacing along nozzle contour.

All the values stay roughly between the accepted range from 30 to 300, although larger node spacing generates larger spans in y^+. Both the enhanced wall functions in the epsilon and the shear stress transport functions in the omega models are considered y^+ insensitive, so accurate solutions can be predicted regardless of near wall grid spacing assuming the above specified values are respected. Increasing grid density near the wall is possible and can allow inner layer effects to be captured in the grid; however, this often leads to elements with high aspect ratios which do not map easily using the fluent cell center calculations. See the results sections for a verification of this insensitivity. Thus, the solution is not and should not be entirely grid independent in the boundary layer. The plots of Mach number along the center axis indicate that the solution is grid independent in the free stream for all the cases calculated.

7.6 Results

The calculation results show excellent agreement in the free stream for all mesh densities; however, better agreement is seen in the surface heat transfer coefficient as the y+ values become optimal in the throat region.

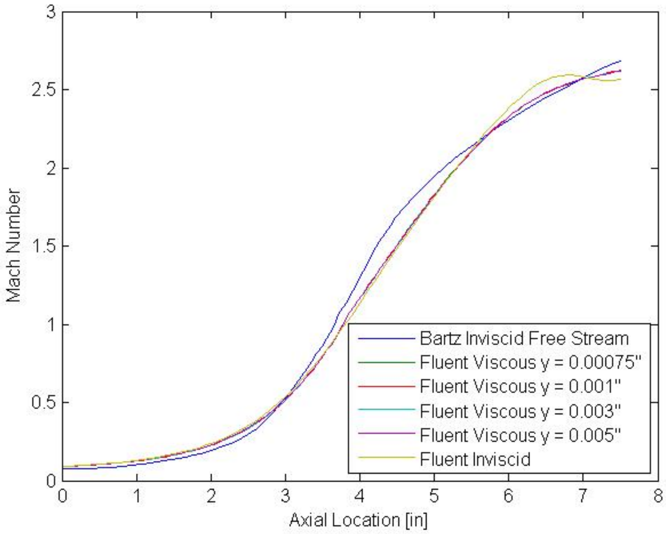

Figure 47. Comparison of axial Mach numbers across 1-D simulation free stream velocities, Fluent inviscid modeling, and Fluent viscous modeling with various first node locations. The inviscid simulation was used for initial solver setup and may not represent a grid independent solution.

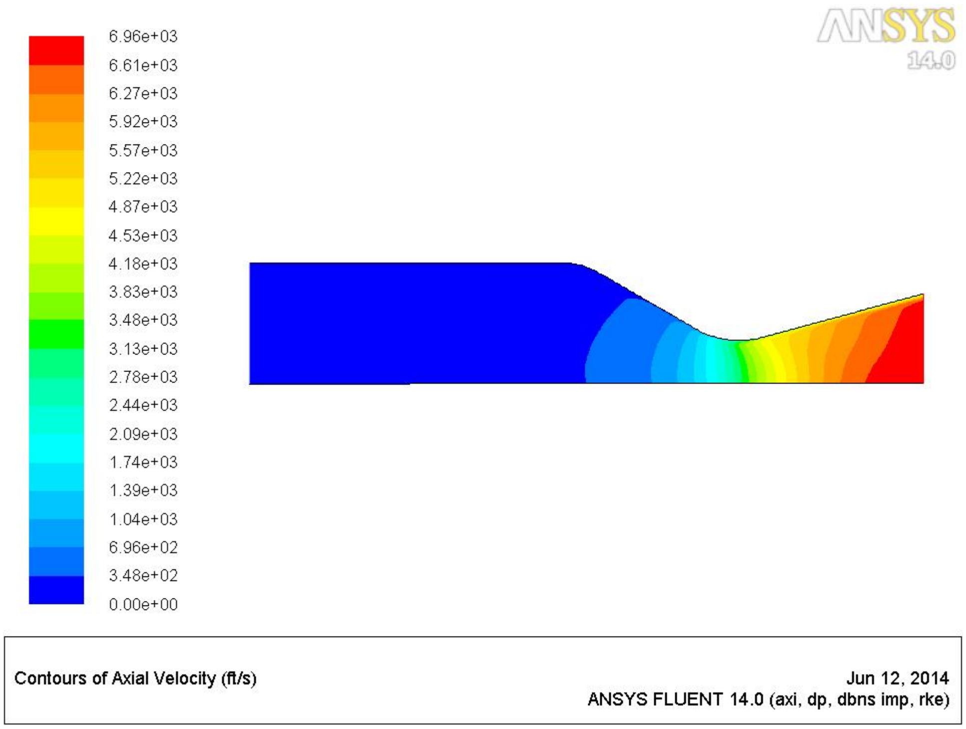

Figure 48. Contours of axial velocity for the FLUENT y = 0.001" case. Notice how thin the wall effected region is and that the lines of constant velocity are not perpendicular to the axis.

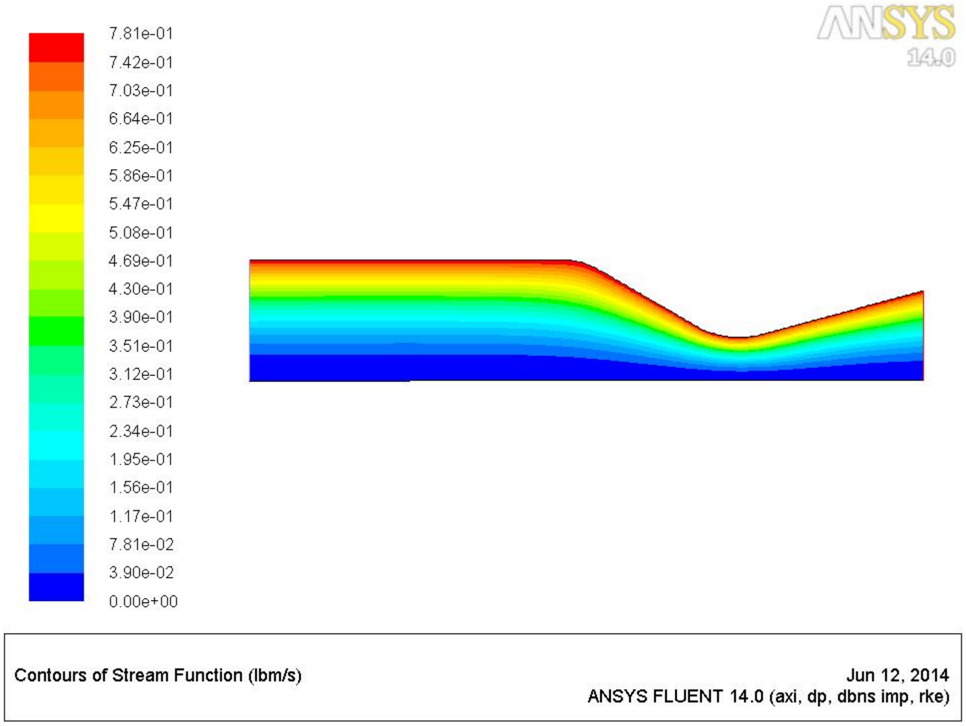

Figure 49. Contours of the stream functions for the FLUENT y = 0.001" case showing that the flow does not recirculate or separate.

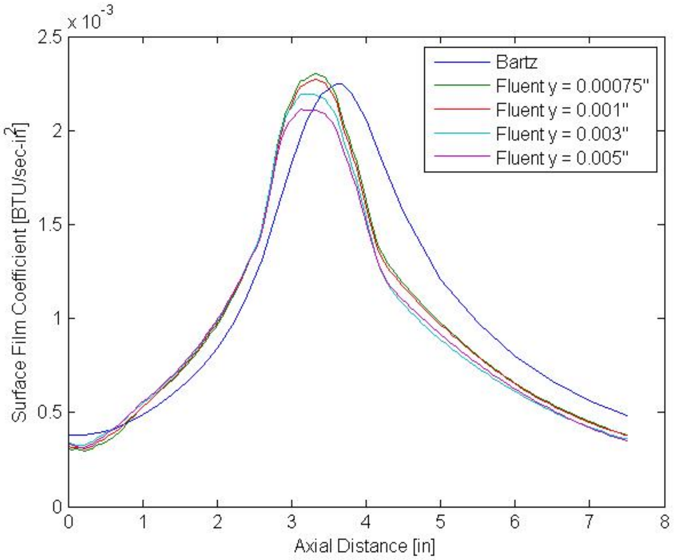

Figure 50. Comparison of surface heat transfer coefficients across 3 grid configuration in FLUENT and the 1-D Bartz simulation results. Note that the lower resolution grids produce slightly lower values of heat flux at the throat since; however, decent agreement is seen across all grids.

The apparent axial shift seen in Figure 49 can likely be attributed to a difference in initial conditions entering the nozzle section or viscous effects in the free stream. Since the initial conditions are specified to the 1-D solver in a rather FLUENT incompatible method, the nozzle entrance length was selected such that both solvers could be compared on the same geometry and match the published test case values. Viscous effects in the free stream could result in higher values of heat flux slightly upstream of the throat when compared to the 1-D model which assumes an inviscid free stream.

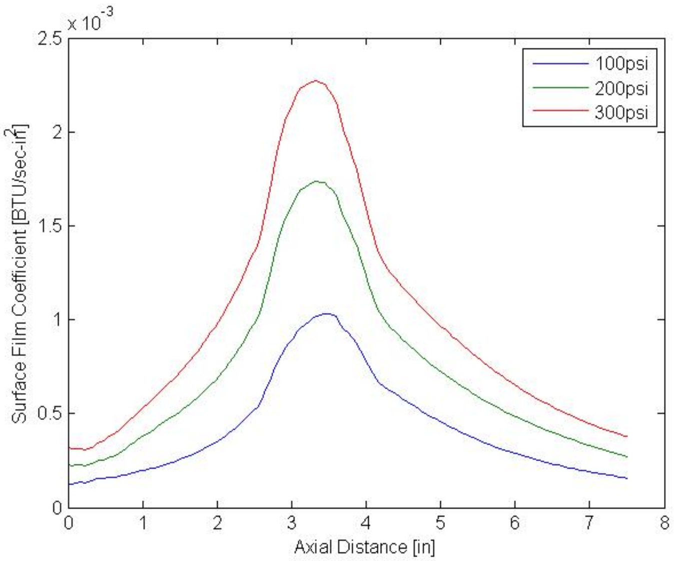

Figure 51. Case study comparison showing surface heat transfer coefficient at three different chamber pressures. Note all other fluid properties, system parameters, and grid dimensions were held constant. The grid was generated with the first node at y = 0.001" from the nozzle contour curve. See Figure 52 for Mach number simulation.

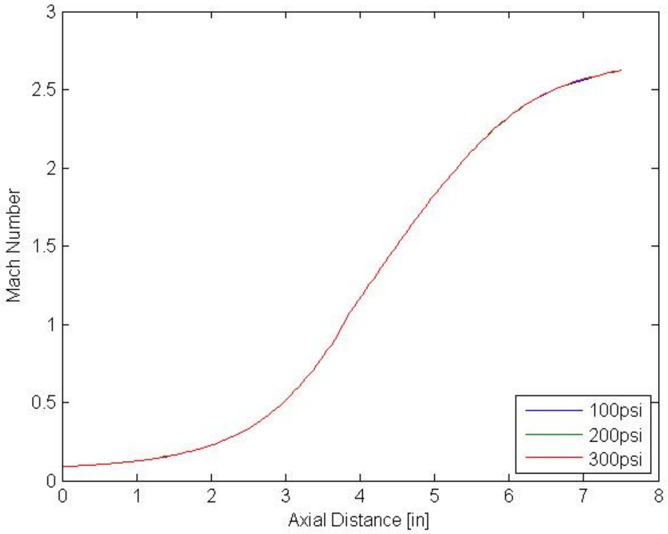

Figure 52. Case study comparison showing Mach number at 3 different chamber pressures. Note that since the flow is chocked at the throat in all cases, the distributions are the same for each operating pressure.

7.7 Discussion

Ultimately, the FLUENT data presented in Figure 49 agrees strongly with the results from the simulation in Reference 1 and thus, the experimental data. Although the raw data available in Figure 43 is not for the exact simulation test case provided it does confirm the trends and orders of magnitude.

The chamber pressure case study produced expected results for Mach number and surface heat transfer coefficient. Decreasing chamber pressure reduced the surface heat transfer coefficient but did not affect the Mach number since the flow is chocked in the throat. With comparable values of velocity in each nozzle, the y^+ values associated with the first node spacing of 0.001" were not observed to change significantly. This permitted using the same mesh throughout the case study.

Complete grid independence cannot be declared for the solution as the value of y^+ for the first node should be kept within the specified range of 30 to 300. Outside critical areas, the lower limit was exceeded although no damages were seen in the results. However, as the upper bound was approached in the throat, divergence from the experimental results and 1-D was observed. The best agreement at the throat section was found when the y^+ values were within the specified range but closest to 30. Further refinement of the grid reduced y^+ at the wall slightly below the recommendation but still produced reasonable results.

8. FUTURE WORK

Although these tests produced reasonable agreement between analytical models and theoretical calculations, the experimental operating points are not typical of most rocket motors. The low chamber pressure limit resulted from a large throat area for fixed fuel grain size and maximum oxidizer flow rate. This rather large throat area was selected in an attempt to perform tests on a geometry that would produce the fewest experimental anomalies; however, if the nozzle entrance diameter was reduced following the fuel grain but before the nozzle, smaller contraction ratios, similar to the ratio used in these tests, could be tested with smaller throat areas. These smaller throat areas significantly increase the range of potential operating points on the Cal Poly Hybrid test stand. Other benefits to reducing the nozzle entrance diameter may include fewer grain effects and the option of a flow conditioning section or post combustion chamber. With strategically designed instrumentation, the resulting smaller nozzles could potentially collect similar data.

Future test apartuses should also have corresponding junctions both axially and theta-wise and multiple junctions at each axial location for further validation. Redundancy in conjunction with a fuel configuration that reaches steady combustion without aggressively heating the nozzle, should produce results that agree across the entire nozzle for a single wall temperature. A complete set of corresponding inner and outer junctions, may be capable of compensating for large variation in outer surface temperature axially. Although the outer temperature should not change substantially during the test interval, the high heat load placed on the nozzle before steady combustion resulted in a large axial variation in inner and outer surface temperatures.

9. CONCLUSION

The series of test performed on the Cal Poly 4:1 nozzle demonstrated that the custom instrumentation and measurement technique is a successful platform for making heat flux measurements. Although ideal conditions to completely validate the Bartz equations are not established on the Cal Poly hybrid test stand, the Bartz model and experimental data agreed well for many stations at different wall temperature. An error analysis demonstrates that the experimental results are accurate within ± 5.2%, which strongly supports the experimental measurements and methods. Taking these results into consideration, the observed differences between experimental and model values are attributed mainly to the nature of the hybrid motor. Experimental measurement error may account for a small amount of these observed differences; however, the bulk of the error is a result of conditions that likely differ from the ideal assumptions in the Bartz model. Ultimately, a robust method of heat flux measurement is developed and various tools for modeling the heat loads on axisymmetric nozzles are presented.

REFERENCES

1. Elliot, David G., Bartz, D. R., and Silver, Sidney. "Calculation of Turbulent Boundary- Layer Growth and Heat Transfer in Axi-Symmetric Nozzles," Technical Report No. 32- 387, Jet Propulsion Laboratory, Pasadena, February 15, 1963.
2. Powell, W. B. Howell, G. W., and Irvin, J.P., "A Method For The Determination of Local Transient Heat Flux in Uncooled Rocket Motors," Technical Report No. 32-257, Jet Propulsion Laboratory, Pasadena, July 1, 1962.
3. Zanstra, P. E. "Welding Uniform Sized Thermocouple Junctions from Thin Wires." *Journal of Physics E: Scientific Instruments* 9.7 (1976): 526-28.
4. Sundqvist, Bertil. "Thermal Diffusivity and Thermal Conductivity of Chromel, Alumel, and Constantan in the Range 100–450 K." *Journal of Applied Physics* 72.2 (1992): 539.
5. Sutton, George Paul. Rocket Propulsion Elements: An Introduction to the Engineering of Rockets. New York: Wiley, 1986.
6. Welsh, W. E. Jr., and A. B. Witte, "A Comparison of Analytical and Experimental Local Heat Fluxes in Liquid-Propellant Rocket Thrust Chambers," Technical Report No. 32-43, Jet Propulsion Laboratory, Pasadena, February 1, 1961.
7. Witte, A. B., and E. Y. Harper, "Experimental Investigation and Empirical Correlation of Local Heat-Transfer Rates in Rocket-Engine Thrust Chambers," Technical Report No. 32-244, Jet Propulsion Laboratory, Pasadena, March 1962.
8. Smithells, Colin J., W. F. Gale, and T. C. Totemeier. *Smithells Metals Reference Book*. Amsterdam: Elsevier Butterworth-Heinemann, 1998.
9. "CEARUN." NASA, Web. <http://www.grc.nasa.gov/WWW/CEAWeb/ceaHome.htm>
10. Netzer, David W. *Hybrid Rocket Internal Ballistics*. Silver Spring: Chemical Propulsion Information Agency, 1972.
11. Zilliac, Greg, and M. Arif Karabeyoglu. *Hybrid Rocket Fuel Regression Rate Data and Modeling*. Proc. of Joint Propulsion COnference, Sacramento, California. AIAA 2006-4504.
12. Pastrone, Dario. "Approaches to Low Fuel Regression Rate in Hybrid Rocket Engines." *International Journal of Aerospace Engineering* 2012 (2012): 1-12.
13. Bartz, D. R. "A Simple Equation for Rapid Estimation of Rocket Nozzle Convective Heat Transfer Coefficients," *Jet Propulsion*, Vol. 27, p. 49, January, 1957.
14. Irvine, Thomas F., R. W. Graham, G. Morrell, R. D. Turnacliff, J. H. Robinson, K. G. Englar, R. G. Deissler, D. R. Bartz, H. N. Mcmanus, and Erich E. Soehngen. "A Six-Part Survey: Rocket Heat-Transfer Literature." *Journal of Heat Transfer* 82.3 (1960): 155.
15. Incropera, Frank P., and David P. DeWitt. *Introduction to Heat Transfer*. New York: Wiley, 1996.
16. White, Frank M. *Viscous Fluid Flow*. 3rd ed. New York: McGraw-Hill, 2005.

APPENDIX A: MATLAB Code to Solve Bartz Equations

Bartz Equation Solver

```
Christopher D'Elia 1/23/2015
This code models the turbulent boundary developing in an axisymmetric
rocket nozzle using the equations presented in Reference 2.
It uses as series of built in MATLAB functions including nonlinear
equation solvers, table interpoalation functions, and first order
differential equation solvers. Parameters are read in from the caseData
structure and an be configured for various products of combustion.
```

Contents

```
function data = BartzSolver(table,caseData)
```

Begin timing the solution process

```
disp('Bartz Solver Elapsed Time: ');
tic
```

Setup and map global variables

```
global gamma c_p r_star FORMII T_0_T T_aw_T_0 a b c zeta_0 m mu_0 rho_U T1 n Pr T_0  op
ts res %zetai
FORMII = table;

T1 = [2.51 0.00590; 3.10 0.00524; 3.97 0.00464; 4.88 0.00426; 5.73 0.00398; 7.41 0.0036
3; 8.94 0.00340; 12.75 0.00308; 16.36 0.00290; 23.2 0.00269; 29.6 0.00255; 35.9 0.00246
; 41.8 0.00238; 53.6 0.00227; 64.8 0.00219];

res = caseData.res;
T_0 = caseData.T_0;
gamma = caseData.gamma;
c_p = caseData.c_p;
p_o = caseData.p_o;
m = caseData.m;
mu_0 = caseData.mu_0;
Pr = caseData.Pr;
phi_0 = caseData.phi_0;
theta_0 = caseData.theta_0;

zeta_0 = 1;
n = 0.1; % Boudary layer interaction exponent
```

Solve for the Mach Number at each axial location

```
[r_star, i] = min(FORMII(:,2));
z_star = FORMII(i,1);

opts = optimset('Tolx', 1e-9);

FORMII(1,4) = fzero(@(x) Mach(x,FORMII(1,2)),0.5, opts);
for i = 2:length(FORMII)
    if(FORMII(i,1)<z_star)
        FORMII(i,4) = fzero(@(x) Mach(x,FORMII(i,2)),0.5, opts);
    elseif(FORMII(i,1)>z_star)
        FORMII(i,4) = fzero(@(x) Mach(x,FORMII(i,2)),FORMII(i-1,4)+0.2, opts);
    else
        FORMII(i,4) = 1;
    end
end
```

Temperature Ratios

```
T_0_T = 1+((gamma-1)/2).*FORMII(:,4).^2;
T_aw_T_0 = (1+(0.89*(gamma-1)/2).*FORMII(:,4).^2)./(1+((gamma-1)/2).*FORMII(:,4).^2);
```

Constants in Integrals

```
a = FORMII(:,3).*T_0_T/T_0;
b = T_0./FORMII(:,3)-1;
c = ((gamma-1)/2*FORMII(:,4).^2)./a;
```

Flow Density

```
rho_U = (32.174/778.2)^0.5*gamma*p_o*FORMII(:,4)./((c_p*T_0*(gamma-1))^0.5*(1+(gamma-1)
/2.*FORMII(:,4).^2).^((gamma+1)/(2*(gamma-1))));
```

Momentum Equation

```
ode_opts = odeset('RelTol', 1e-9);
[z,x] = ode45(@MomentumEnergy,[FORMII(1,1) FORMII(end,1)],[theta_0 phi_0], ode_opts);
```

Finish timing the solution process

```
disp(toc);
```

Post process the data and produce outputs in desired units

```
data = [z,x];
for i = 1:length(z)
    data(i,4) = C_h(C_f(Reynolds(x(i,2),z(i,1)),z(i,1)),x(i,:));
    data(i,5) = C_f(Reynolds(x(i,1),z(i,1)),z(i,1));
    data(i,6) = c_p*rho_Ui(z(i,1))*data(i,4)*1055.05585*39.37*39.37*5/9;
end
data(:,8) = interp1(FORMII(:,1),T_0./T_0_T,data(:,1));
data(:,7) = data(:,6).*(data(:,8)-T_w(z(:,1)))*5/9;



end
```

ODE45 Function for Solving the Momentum Energy Equations

```
function dx = MomentumEnergy(z,x)
    global gamma T_0
    M = Ma(z);
    Tw = T_w(z);
    r = radius(z);
    dx(1,1) = C_f(Reynolds(x(1,1),z),z)/2*(1+drdz(z)^2)^0.5-x(1,1)*((2-M^2+delstheta(z,
x))/M/(1+(gamma-1)/2*M^2)*dMdz(z)+1/r*drdz(z)); %dtheta
    dx(2,1) = C_h(C_f(Reynolds(x(2,1),z),z),x)*((T_aw(z)-Tw)/(T_0-Tw)*(1+drdz(z)^2)^0.5
)-x(2,1)*((1-M^2)/M/(1+(gamma-1)/2*M^2)*dMdz(z)+1/r*drdz(z)-(1/(T_0-Tw)*dT_wdz(z))); %d
phi
end
```

Evaluate the Reynolds number based on a given parameter and z location

```
function R = Reynolds(param,z)
    global mu_0 gamma m
    R = (12/32.174)*(rho_Ui(z)*param/mu_0)*(1+(gamma-1)/2*Ma(z)^2)^m;
end
```

Evaluate C_f based on Reynolds number

```
function Cf = C_f(R,z)
    global m opts
    Cfb = T1i(R);
    if(Cfb*R>64.8)
        Cfb = fminbnd(@(x) minimize40(x,R),0,0.00219, opts);
    end
    if(Cfb*R<=2.51)
        Cfb = solve41(R);
    end
    Cf  = Cfb/((0.5*(ai(z)+1))^((3-m)/4));
end
```

Solve Equation 41 for Cf

```
function result = solve41(R)
    result = (0.009896/(R^0.562))^(1/1.562);
end
```

Solve Equation 40 for Cf

```
function error = minimize40(Cf,R)
    error = 2.44*log(Cf*R/(Cf*(3.781-25.104/(2/Cf)^0.5)))+7.68-(2/Cf)^0.5;
end
```

Interp and solve for Cf using Table 1 data

```
function result = T1i(R)
    global T1
    result = interp1(T1(:,1)./T1(:,2),T1(:,2),R,'cubic');
end
```

Evaluate Equation 47 for the Stanton Number

```
function c = C_h(Cf,x)
    global n Pr
    c = (Cf/2*(x(2)/x(1))^n)/(1-5*((Cf/2)^0.5)*(1-Pr+log(6/(5*Pr+1))));
end
```

Evaluate the throat boundary layer thickness over the momentum thickness

```
function d = delstheta(z,x)
    global zeta_0 opts
    a = ai(z);
    b = bi(z);
    c = ci(z);
    zeta = fzero(@(ze) minimizeZeta(ze,b,c,x),zeta_0, opts);
    if(zeta>=1)
        d = ((a*zeta^7)/7-I2(b,c,zeta)-I3(b,c,zeta))/I1(b,c,zeta);
    else
        d = (a/7-I6(b,c,zeta)-I7(b,c,zeta))/(I4(b,c,zeta)+I5(b,c,zeta));
    end
    zeta_0 = zeta;
end
```

Solve for zeta, the shape parameter

```
function error = minimizeZeta(zeta,b,c,x)
    if(zeta>=1)
        error = ((x(2)*I1(b,c,zeta)/x(1)/(I2p(b,c,zeta)+I3p(b,c,zeta)/zeta))-zeta^8);
    else
        error = ((x(2)*(I4(b,c,zeta)+I5(b,c,zeta))/x(1)/I1p(b,c,zeta))-zeta^8);
    end
end
```

Mach Number Equation 50

```
function error = Mach(M,r)
    global gamma r_star
    error = (1/M)*((1+(gamma-1)/2*M^2)/((gamma+1)/2))^((gamma+1)/(2*(gamma-1)))-(r/r_st
ar)^2;
end
```

Integral 1

```
function I = I1(b,c,zeta)
    global res
    s = 0:1/res:1;
    I = trapz(s,s.^7.*(1-s)./(1+b/zeta.*s-c*s.^2));
end
```

Integral 2

```
function I = I2(b,c,zeta)
    global res
    s = 0:1/res:1;
    I = trapz(s,s.^7./(1+b/zeta.*s-c*s.^2));
end
```

Integral 3

```
function I = I3(b,c,zeta)
    global res
    s = 1:(zeta-1)/res:zeta;
    I = trapz(s,s.^6./(1+b/zeta.*s-c));
end
```

Integral 4

```
function I = I4(b,c,zeta)
    global res
    s = 0:zeta/res:zeta;
    I = trapz(s,s.^7.*(1-s)./(1+b/zeta.*s-c*s.^2));
end
```

Integral 5

```
function I = I5(b,c,zeta)
    global res
    s = zeta:(1-zeta)/res:1;
    I = trapz(s,s.^7.*(1-s)./(1+b-c*s.^2));
end
```

Integral 6

```
function I = I6(b,c,zeta)
    global res
    s = 0:zeta/res:zeta;
    I = trapz(s,s.^7./(1+b/zeta.*s-c*s.^2));
end
```

Integral 7

```
function I = I7(b,c,zeta)
    global res
    s = zeta:(1-zeta)/res:1;
    I = trapz(s,s.^7./(1+b-c*s.^2));
end
```

Integral 1'

```
function I = I1p(b,c,zeta)
    global res
```

```
    s = 0:1/res:1;
    I = trapz(s,s.^7.*(1-s)./(1+b.*s-c*(zeta^2)*s.^2));
end
```

Integral 2'

```
function I = I2p(b,c,zeta)
    global res
    s = 0:1/zeta/res:1/zeta;
    I = trapz(s,s.^7.*(1-s)./(1+b.*s-c*zeta^2*s.^2));
end
```

Integral 3'

```
function I = I3p(b,c,zeta)
    global res
    s = 1/zeta:(1-1/zeta)/res:1;
    I = trapz(s,s.^6.*(1-s)./(1+b.*s-c));
end
```

Compute the deriv dr/dz

```
function d = drdz(z)
    global FORMII
    d = ppval(fnder(interp1(FORMII(:,1),FORMII(:,2),'cubic','pp')),z);
end
```

Compute the deriv dM/dz

```
function d = dMdz(z)
    global FORMII
    d = ppval(fnder(interp1(FORMII(:,1),FORMII(:,4),'cubic','pp')),z);
end
```

Compute the deriv dT_w/dz

```
function d = dT_wdz(z)
    global FORMII
    d = ppval(fnder(interp1(FORMII(:,1),FORMII(:,3),'cubic','pp')),z);
end
```

Interp Ma

```
function M = Ma(z)
    global FORMII
    M = interp1(FORMII(:,1),FORMII(:,4),z,'cubic');
end
```

Interp r

```
function r = radius(z)
    global FORMII
    r = interp1(FORMII(:,1),FORMII(:,2),z,'cubic');
end
```

Interp T_w

```
function T = T_w(z)
    global FORMII
    T = interp1(FORMII(:,1),FORMII(:,3),z,'cubic');
end
```

Interp T_aw

```
function T = T_aw(z)
    global T_aw_T_0 FORMII T_0
    T = interp1(FORMII(:,1),T_aw_T_0,z,'cubic')*T_0;
end
```

Interp a

```
function constant = ai(z)
    global a FORMII
    constant = interp1(FORMII(:,1),a,z,'cubic');
end
```

Interp b

```
function constant = bi(z)
    global b FORMII
    constant = interp1(FORMII(:,1),b,z,'cubic');
end
```

Interp c

```
function constant = ci(z)
    global c FORMII
    constant = interp1(FORMII(:,1),c,z,'cubic');
end
```

Interp flowDensity

```
function flowDensity = rho_Ui(z)
    global rho_U FORMII
    flowDensity = interp1(FORMII(:,1),rho_U,z,'cubic');
end
```

Published with MATLAB® 7.10

APPENDIX B: MATLAB Code for Processing Raw Data Files

Process Raw Data

```
Christopher D'Elia 1/23/2015
This code processes raw data taken on the Cal Poly Hybrid Rocket stand.
All the data is resampled according to a specified increment over a
specificed interval. The outer junction temperatures are interpolated to
produce 12 paired data streams for each axial station. Inner surface
junction temperatures are plotted as a function of time to display the
raw data.
```

Contents

- Map system parameters
- Open the raw data files
- Process and correct the time stamps
- Resample the data according to the user input
- Interpolate to determine the odd outerjunction temperatures
- Offset the time to start at 0s
- Plot the raw data

```
function processDataV2(fileNames,dataFile,start,stop,fluxConst,geoConst)
```

Map system parameters

```
step = fluxConst.dt;
z_throat = geoConst.z_throat;
```

Open the raw data files

```
fid{1} = fopen(fileNames{1});
fid{2} = fopen(fileNames{2});
fid{3} = fopen(fileNames{3});

data1 = textscan(fid{1}, '%s %f %f %f %f %f %f %f %f %f %f %f %f %f %f %f','Headerlines
',2,'Delimiter',',');
data2 = textscan(fid{2}, '%s %f %f %f %f %f %f %f %f %f %f %f %f %f %f %f','Headerlines
',2,'Delimiter',',');
data3 = textscan(fid{3}, '%s %f %f %f %f %f %f %f %f','Headerlines',2,'Delimiter',',');

fclose(fid{1});
fclose(fid{2});
fclose(fid{3});
```

Process and correct the time stamps

```
time1 = zeros(length(data1{1,1}),1);
time2 = zeros(length(data2{1,1}),1);
time3 = zeros(length(data3{1,1}),1);

for i = 1:length(data1{1,1})
    if length(data1{1,1}{i,1}) == 11
        data1{1,1}{i,1} = [data1{1,1}{i,1}(1:9), '0',data1{1,1}{i,1}(10:end)];
    end
    seconds = str2double(data1{1,1}{i,1}(7:end));
    minutes = str2double(data1{1,1}{i,1}(4:5));
    time1(i) = minutes*60 + seconds;
end

for i = 1:length(data2{1,1})
    if length(data2{1,1}{i,1}) == 11
        data2{1,1}{i,1} = [data2{1,1}{i,1}(1:9), '0',data2{1,1}{i,1}(10:end)];
```

```
    end
    seconds = str2double(data2{1,1}{i,1}(7:end));
    minutes = str2double(data2{1,1}{i,1}(4:5));
    time2(i) = minutes*60 + seconds;
end

for i = 1:length(data3{1,1})
    if length(data3{1,1}{i,1}) == 11
        data3{1,1}{i,1} = [data3{1,1}{i,1}(1:9), '0',data3{1,1}{i,1}(10:end)];
    end
    seconds = str2double(data3{1,1}{i,1}(7:end));
    minutes = str2double(data3{1,1}{i,1}(4:5));
    time3(i) = minutes*60 + seconds;
end
```

Resample the data according to the user input

```
time = start:step:stop;

innerSurfaceTemps{1} = interp1(time2,data2{1,15},time)';
innerSurfaceTemps{2} = interp1(time2,data2{1,16},time)';
innerSurfaceTemps{3} = interp1(time1,data1{1,2},time)';
innerSurfaceTemps{4} = interp1(time1,data1{1,3},time)';
innerSurfaceTemps{5} = interp1(time1,data1{1,4},time)';
innerSurfaceTemps{6} = interp1(time1,data1{1,5},time)';
innerSurfaceTemps{7} = interp1(time1,data1{1,6},time)';
innerSurfaceTemps{8} = interp1(time1,data1{1,7},time)';

innerSurfaceTemps{9} = interp1(time1,data1{1,8},time)';
innerSurfaceTemps{10} = interp1(time1,data1{1,9},time)';
innerSurfaceTemps{11} = interp1(time3,data3{1,4},time)';
innerSurfaceTemps{12} = interp1(time3,data3{1,5},time)';

outerSurfaceTemps{2} = interp1(time3,data3{1,6},time)';
outerSurfaceTemps{4} = interp1(time3,data3{1,7},time)';
outerSurfaceTemps{6} = interp1(time3,data3{1,8},time)';
outerSurfaceTemps{8} = interp1(time3,data3{1,9},time)';
outerSurfaceTemps{10} = interp1(time1,data1{1,10},time)';
outerSurfaceTemps{12} = interp1(time1,data1{1,11},time)';

scale = interp1(time1,data1{1,16},time)';
pressure = interp1(time2,data2{1,4},time)';
```

Interpolate to determine the odd outerjunction temperatures

```
for i = 1:2:11
    for j = 1:length(time)
        measuredOuter = [outerSurfaceTemps{2}(j,1),outerSurfaceTemps{4}(j,1),outerSurfa
ceTemps{6}(j,1),outerSurfaceTemps{8}(j,1),outerSurfaceTemps{10}(j,1),outerSurfaceTemps{
12}(j,1)];
        outerSurfaceTemps{i}(j,1) = interp1(z_throat(2:2:12),measuredOuter,z_throat(i),
'linear','extrap');
    end
end
```

Offset the time to start at 0s

```
time = time-time(1);
```

Plot the raw data

```
h = figure;
plot(time,innerSurfaceTemps{1},time,innerSurfaceTemps{2},...
    time,innerSurfaceTemps{3},time,innerSurfaceTemps{4},...
```

```
    time,innerSurfaceTemps{5},time,innerSurfaceTemps{6})
xlabel('Time [s]')
ylabel('Surface Junction Temerature [F]')
legend('Junction 1','Junction 2','Junction 3','Junction 4','Junction 5','Junction 6')
saveas(h,'tempTime1','jpg')

h = figure;
plot(time,innerSurfaceTemps{7},time,innerSurfaceTemps{8},...
    time,innerSurfaceTemps{9},time,innerSurfaceTemps{10},...
    time,innerSurfaceTemps{11},time,innerSurfaceTemps{12})
xlabel('Time [s]')
ylabel('Surface Junction Temerature [F]')
legend('Junction 7','Junction 8','Junction 9','Junction 10','Junction 11','Junction 12'
,'location','NorthWest')
saveas(h,'tempTime2','jpg')
save(dataFile, 'outerSurfaceTemps', 'innerSurfaceTemps', 'scale', 'time','pressure');


end
```

Published with MATLAB® 7.10

APPENDIX C: MATLAB Code for Compiling System Parameters

MASTER ROCKET DATA PROCESSOR

Christopher D'Elia 1/23/2015
This code initializes all the system parameters used in the subsequent
files and manages the data processed by each individual file.

Contents

Clear the playing field

```
clc
clear all
close all
```

Initialize constants for computeHeatFlux()

```
fluxConst.dt = 0.05; % Time Step dt [s]
fluxConst.dr = 0.05/39.3701; % Radial Step dr [m]
fluxConst.rho = 7.86*(100^3)/1000; % Steel Density [kg/m3]

fluxConst.r_inner = fliplr([1.601,1.590,1.437,1.087,0.905,0.845,0.826,...
    0.846,0.939,1.043,1.181,1.320])/39.3701; % [m]
fluxConst.r_thick = fliplr([0.5,0.504,0.545,0.634,0.542,0.510,0.5,...
    0.508,0.518,0.518,0.518,0.518])/39.3701; % [m]
fluxConst.k_table(:,1) = [100 200 400 600 800 1000]'; % [C]
fluxConst.k_table(:,2) = [51.1 49.0 42.7 35.6 26.0 27.2]'; % [W/m/K]
fluxConst.cp_table(:,1) = fluxConst.k_table(:,1); % [C]
fluxConst.cp_table(:,2) = [0.486, 0.520, 0.599,...
    0.749, 0.950, 0.950]'*1000; % [J/kg/K]
fluxConst.setBack = 0.0226/39.3701; %[m]
fluxConst.i1 = 190*(0.05/fluxConst.dt); % Starting Index
fluxConst.i2 = 230*(0.05/fluxConst.dt); % Stopping Index

fluxConst.cp = min(fluxConst.cp_table(:,2)); % [J/kg/K]
fluxConst.k = max(fluxConst.k_table(:,2)); % [W/m/K]
```

Initialize constants for BartzSolver()

```
visc = [0.94874  0.91532  0.79915]*2.08854342332e-6; % [lbf-s/ft2]
visc = visc/visc(1);
Tv = [3054.83  2901.21  2376.28]*9/5; % [K]
Tvn = Tv/Tv(1);
fit = polyfit(log(Tvn),log(visc),1);

BartzConst.res = 50; % Integration resolution
BartzConst.T_0 = Tv(1);
BartzConst.gamma = 1.13;
BartzConst.c_p = 4.78*0.238845896627;
BartzConst.m = fit(1);
BartzConst.mu_0 = 0.94583*2.08854342332e-6;
BartzConst.Pr = 0.48;
```

```
BartzConst.phi_0 = 0.001;
BartzConst.theta_0 = 0.001;
```

Initialize constants for nozzleGeo()

```
geoConst.top = 1+4.492;
geoConst.numPts = 50;
geoConst.r1 = 1.594;
geoConst.r2 = 1.593;
geoConst.divth = deg2rad(15);
geoConst.shoulderLength = 1;
geoConst.r1Length = 1.053;
geoConst.r2Length = 1.466;
geoConst.throat = 0.797;
geoConst.start2throat = 2.107;
geoConst.z_throat = [2,1.5,1,0.625,0.25,0,-0.25,-0.5,-0.875,...
    -1.375,-1.875,-2.375]; %[in]
```

Load all data into .mat

```
processDataV2({'ABCD_RocketData032-1.log','ABCD_RocketData032-2.log',...
    'ABCD_RocketData032-3.log'},'Run104Data',1570,1585,fluxConst,geoConst);
```

Calculate film coeff

```
[q_out, T_out] = computeHeatFlux('Run104Data.mat',3,fluxConst);
```

Compute mean values

```
[q_exp,T_mean,P_mean] = computeMeanValues('Run104Data.mat',q_out,T_out,...
    fluxConst.i1,fluxConst.i2);
```

Compute nozzle geometry

```
[table] = nozzleGeo((T_mean+273.15)*9/5,geoConst);
```

Determine experimental heat flux

```
temp = 500+460; % [R]
q_exp = plotFluxTemp(fluxConst,[1:12],q_out,(T_out+275.15)*9/5,temp);
```

Compute Bartz solution

```
table(:,3) = temp; %[R]
BartzConst.p_o = P_mean+14.696; % [psia]

data = BartzSolver(table,BartzConst);
```

Published with MATLAB® 7.10

Compute Heat Flux

```
Christopher D'Elia 1/23/2015
This code uses finite difference equations to compute the heat flux into
an axisymmetric hybrid rocket nozzle at 12 individual stations.
Temperature dependent properties and other system parameters are loaded
in before the parallel processing toolbox is used to share the work
between any specified number of labs.
```

Contents

```
function [q_out,T_out] = computeHeatFlux(dataFile,par_num,fluxConst)
```

Load the system parameters from the fluxConst structure

```
dt = fluxConst.dt;
dr = fluxConst.dr;
rho = fluxConst.rho;
cp = fluxConst.cp;
k = fluxConst.k;
r_inner = fluxConst.r_inner;
r_thick = fluxConst.r_thick;
k_table = fluxConst.k_table;
cp_table = fluxConst.cp_table;
setBack = fluxConst.setBack;
```

Load the raw data

```
load(dataFile);
t = time;
```

Check the stability of the finite difference equations

```
stable = k*dt/rho/cp/(dr^2);

if stable <= 0.5
    disp('Stable');
    disp(stable)
else
    disp('Unstable');
    disp(stable)
    return
end
```

Loop over the specified axial stations and compute the internal

temperature distribution

```
matlabpool(par_num)
parfor z = 1:length(r_inner)

    Ti = (innerSurfaceTemps{z}-32)*5/9; % [C]
    To = (outerSurfaceTemps{z}-32)*5/9; % [C]
```

```
    rthick = r_thick(z);
    rinner = r_inner(z);
    router = rthick+rinner;
    r = rinner+setBack:dr:router;

    T = zeros(length(t),length(r));
    T(:,1) = Ti;
    T(:,end) = To;
    T(1,:) = linspace(Ti(1,1),To(1,1),length(r));
    q = zeros(length(t),1);
    Tw = zeros(length(t),1);
    for i = 1:length(t)-1
        for j = 2:length(r)-1
            cp = interp1(cp_table(:,1),cp_table(:,2),T(i,j),'cubic',cp_table(1,2));
            kij = interp1(k_table(:,1),k_table(:,2),T(i,j),'cubic',k_table(1,2));
            kijp = interp1(k_table(:,1),k_table(:,2),T(i,j+1),'cubic',k_table(1,2));
            kijm = interp1(k_table(:,1),k_table(:,2),T(i,j-1),'cubic',k_table(1,2));

            T(i+1,j) = T(i,j) + dt/2/(dr^2)/rho/cp*(((kijp+kij)*(T(i,j+1)-T(i,j))...
                -(kij+kijm)*(T(i,j)-T(i,j-1))+dr*kij/r(j)*(T(i,j+1)-T(i,j-1))));
        end

        cf = fit(r',T(i+1,:)','exp2');
        Tw(i+1) = cf.a*exp(cf.b*rinner)+cf.c*exp(cf.d*rinner);
        ks = interp1(k_table(:,1),k_table(:,2),Tw(i+1),'cubic',k_table(1,2));
        dTdr = cf.a*cf.b*exp(cf.b*rinner)+cf.c*cf.d*exp(cf.d*rinner);
        q(i+1) = -ks*dTdr;
    end

    h=figure(1);
    surfc(t,r,T','EdgeColor','none','LineStyle','none')
    xlabel('Time [s]')
    ylabel('Radius [m]')
    zlabel('Temperature [^{\circ}C]')
    view([-135,45])
    saveas(h,sprintf('station %i temp',z),'jpg');

    h = figure(2);
    plot(t,q(:));
    xlabel('Time [s]')
    ylabel('Heat Flux [W/m^2-K]')
    saveas(h,sprintf('station %i flux',z),'jpg');

    q_out(:,z) = q;
    T_out(:,z) = Tw;
end

matlabpool close


end
```

Published with MATLAB® 7.10

Compute Mean Values

```
Christopher D'Elia 1/23/15
This code computes the necessary mean values for the remainder of the
data processing tasks.
```

Contents

- Load the raw data
- Average the computed wall temperature, computed heat flux, and pressure
- Plot the pressure

```
function [q_mean,T_mean,P_mean] = computeMeanValues(dataFile,q_out,T_out,start,stop)
```

Load the raw data

```
load(dataFile)
```

Average the computed wall temperature, computed heat flux, and pressure

```
for z = 1:min(size(q_out))
    q_mean(z) = mean(q_out(start:stop,z));
    T_mean(z) = mean(T_out(start:stop,z));
end

P_mean = mean(pressure(start:stop));
```

Plot the pressure

```
h = figure;
plot(time,pressure)
xlabel('Time [s]');
ylabel('Chamber Pressure [psi]');
saveas(h,'pressure','jpg')


end
```

Published with MATLAB® 7.10

Nozzle Geometry Developer

```
Christopher D'Elia 1/23/15
This code develops the 2-D profile of an axisymmetric nozzle with
specified parameters given in geoConst for the number of points
specified.
```

```
function [table] = nozzleGeo(T_mean,geoConst)

z = linspace(0,geoConst.top,geoConst.numPts);
r = zeros(geoConst.numPts,1);
for i = 1:length(z)
    if z(i)<=geoConst.shoulderLength
        r(i) = geoConst.r1;
    elseif z(i)<=geoConst.shoulderLength+geoConst.r1Length
        r(i) = sqrt(geoConst.r1^2-(z(i)-geoConst.shoulderLength)^2);
    elseif z(i)<=geoConst.shoulderLength+geoConst.r1Length+geoConst.r2Length
        r(i) = geoConst.r2+geoConst.throat-...
            sqrt(geoConst.r2^2-...
            (geoConst.shoulderLength+geoConst.start2throat-z(i))^2);
    else
        r(i) = atan(geoConst.divth)*(z(i)-...
            geoConst.shoulderLength-...
            geoConst.r1Length-geoConst.r2Length)+0.851;
    end
end

z = z-geoConst.start2throat-geoConst.shoulderLength;

temps = interp1(geoConst.z_throat,T_mean,z,'linear','extrap');

table(:,1) = z;
table(:,2) = r;
table(:,3) = temps;

end
```

Published with MATLAB® 7.10

Plot Heat Flux Versus Wall Temperature

```
Christopher D'Elia 11/23/2015
This code computes the linear correlations between heat flux and wall
temperautre and plots the heat flux verus wall temperature. The function
returns the heat flux given a specific wall temperature
```

```
function qConstantWallTemp = plotFluxTemp(fluxConst,stations,q,T,temp)

colors = {'c' 'm' 'r' 'k' 'r' 'g' 'b' '--c' '--m' '--r' '--k' '--g'};
h = figure;
hold on
for i = stations
    plot(T(fluxConst.i1:fluxConst.i2,i),q(fluxConst.i1:fluxConst.i2,i),colors{i})
    qLinFit{i} = polyfit(T(fluxConst.i1:fluxConst.i2,i),q(fluxConst.i1:fluxConst.i2,i),
1);
    qConstantWallTemp(i) = polyval(qLinFit{i},temp);
end
hold off
xlabel('Wall Temperature [R]');
ylabel('Heat Flux [W/m^2]')
legend('Station 1','Station 2','Station 3','Station 4','Station 5','Station 6',...
    'Station 7','Station 8','Station 9','Station 10','Station 11','Station 12','locatio
n','SouthEast')
box on
saveas(h,'fluxTemp','jpg')
end
```

Published with MATLAB® 7.10